

Spin-current-mediated rapid magnon localisation and coalescence after ultrafast optical pumping of ferrimagnetic alloys

IACOCCA, Ezio, LIU, T.M., REID, A.H., FU, Z., RUTA, S, GRANITZKA, P.W., JAL, E, BONETTI, S., GRAY, A.X., GRAVES, C.E., KUKREJA, R., CHEN, Z., HIGLEY, D.J., CHASE, T., LE GUYADER, L., HIRSCH, K., OHLDAG, H., SCHLOTTER, W.F., DAKOVSKI, G.L., COSLOVICH, G., HOFFMANN, M.C., CARRON, S., TSUKAMOTO, A., KIRILYUK, A., KIMEL, A.V., RASING, T.H., STOHR, J., EVANS, R.F.L., OSTLER, Thomas <<http://orcid.org/0000-0002-1328-1839>>, CHANTRELL, R.W., HOEFER, M.A., SILVA, T.J. and DURR, H.A.

Available from Sheffield Hallam University Research Archive (SHURA) at:

<https://shura.shu.ac.uk/24240/>

This document is the Accepted Version [AM]

Citation:

IACOCCA, Ezio, LIU, T.M., REID, A.H., FU, Z., RUTA, S, GRANITZKA, P.W., JAL, E, BONETTI, S., GRAY, A.X., GRAVES, C.E., KUKREJA, R., CHEN, Z., HIGLEY, D.J., CHASE, T., LE GUYADER, L., HIRSCH, K., OHLDAG, H., SCHLOTTER, W.F., DAKOVSKI, G.L., COSLOVICH, G., HOFFMANN, M.C., CARRON, S., TSUKAMOTO, A., KIRILYUK, A., KIMEL, A.V., RASING, T.H., STOHR, J., EVANS, R.F.L., OSTLER, Thomas, CHANTRELL, R.W., HOEFER, M.A., SILVA, T.J. and DURR, H.A. (2019). Spin-current-mediated rapid magnon localisation and coalescence after ultrafast optical pumping of ferrimagnetic alloys. *Nature communications*, 10 (1756). [Article]

Copyright and re-use policy

See <http://shura.shu.ac.uk/information.html>

1 **Spin-current-mediated rapid magnon localisation and coalescence after**
2 **ultrafast optical pumping of ferrimagnetic alloys**

3 E. Iacocca^{1,2,3}, T-M. Liu⁴, A. H. Reid⁴, Z. Fu⁵, S. Ruta⁶, P. W. Granitzka⁴, E. Jal⁴, S. Bonetti⁴,
4 A. X. Gray^{4,7}, C. E. Graves⁴, R. Kukreja⁴, Z. Chen⁴, D. J. Higley⁴, T. Chase⁴, L. Le
5 Guyader^{4,8}, K. Hirsch⁴, H. Ohldag⁴, W. F. Schlotter⁴, G. L. Dakovski⁴, G. Coslovich⁴, M. C.
6 Hoffmann⁴, S. Carron⁴, A. Tsukamoto⁹, A. Kirilyuk¹⁰, A. V. Kimel¹⁰, Th. Rasing¹⁰, J. Stöhr⁴,
7 R. F. L. Evans⁶, T. Ostler^{11,12}, R. W. Chantrell^{6,10}, M. A. Hofer¹, T. J. Silva², H. A. Dürr^{4,13}

8 ¹ Department of Applied Mathematics, University of Colorado, Boulder, CO 80309, USA

9 ² National Institute of Standards and Technology, Boulder, CO 80305, USA

10 ³ Department of Physics, Division for Theoretical Physics, Chalmers University of
11 Technology, Gothenburg 412 96, Sweden

12 ⁴ SLAC National Accelerator Laboratory, 2575 Sand Hill Road, Menlo Park, CA 94025,
13 USA

14 ⁵ School of Physics, Science, and Engineering, Tongji University, Shanghai 200092, China

15 ⁶ Department of Physics, University of York, York YO10 5DD, UK.

16 ⁷ Department of Physics, Temple University, 1925 N. 12th St. Philadelphia, PA 19122, USA

17 ⁸ Spectroscopy & Coherent Scattering, European X-Ray Free-Electron Laser Facility
18 GmbH, Holzkoppel 4, 22869 Schenefeld, Germany

19 ⁹ Department of Electronics and Computer Science, Nihon University, 7-24-1 Narashino-dai
20 Funabashi, Chiba 274-8501, Japan

21 ¹⁰ Radboud University, Institute for Molecules and Materials, Heyendaalseweg 135, 6525 AJ
22 Nijmegen, The Netherlands

23 ¹¹ Université de Liège, Physique des Matériaux et Nanostructures, Liège B-4000 Sart
24 Tilman, Belgium

25 ¹² Faculty of Arts, Computing, Engineering and Sciences, Sheffield Hallam University,
26 Howard Street, Sheffield, S1 1WB, UK

27 ¹³ Department of Physics and Astronomy, Uppsala University, Box 516, 751 20 Uppsala,
28 Sweden

29 Corresponding author: H. A. Dürr, hermann.durr@physics.uu.se

30

31 **Sub-picosecond magnetisation manipulation via femtosecond optical pumping has**
32 **attracted wide attention ever since its original discovery in 1996. However, the spatial**
33 **evolution of the magnetisation is not yet well understood, in part due to the difficulty in**
34 **experimentally probing such rapid dynamics. Here, we find evidence of a universal**
35 **rapid magnetic order recovery in ferrimagnets with perpendicular magnetic anisotropy**
36 **via nonlinear magnon processes. We identify magnon localisation and coalescence**
37 **processes, whereby localised magnetic textures nucleate and subsequently interact and**
38 **grow in accordance with a power law formalism. Simulations indicate that the**
39 **appearance of noncollinear magnetisation via optical pumping establishes exchange-**
40 **mediated spin currents with an equivalent 100% spin polarised charge current density**
41 **of 10^7 A cm⁻². Such large spin currents precipitate rapid recovery of magnetic order**
42 **after optical pumping. The magnon processes discussed here provide new insights for**
43 **the stabilization of desired meta-stable states.**

44

45 Spin dynamics upon femtosecond optical pumping [1-15] have been intensely studied
46 during the last two decades both because of potential applications for information storage and
47 because of the need to understand the fundamental physics involved [16]. A variant of these
48 dynamics is all-optical switching (AOS). While originally demonstrated for ferrimagnetic
49 alloys with perpendicular magnetic anisotropy (PMA) [2], AOS has been reported to occur in
50 ferromagnetic PMA materials subject to optical pumping [9-12] or by use of ultrafast hot
51 electrons [14, 15, 17]. Whereas the picosecond magnetisation dynamics, even for non-
52 uniform states [5, 6], has been successfully modelled with spatially averaged, quasi-
53 equilibrium models [1, 3, 4, 18] there is a growing understanding of the important role of
54 spatially-varying magnetisation. For example, the chemical inhomogeneity of amorphous
55 ferrimagnetic GdFeCo alloys results in picosecond transfer of angular momentum that both
56 drives magnetisation switching [8] and influences the equilibrium state after pumping with a
57 single laser pulse [13]. More recently, the effective domain size during cooling has been
58 identified as a criterion to predict whether macroscopic AOS can occur [12].

59 To further investigate the fundamental physics involved in the evolution of spatially
60 varying magnetisation after ultrafast optical pumping, and to elucidate which physical
61 mechanisms are most important for the recovery of local magnetic order at picosecond
62 timescales, we study the space- and time-dependent magnetisation dynamics in ferrimagnetic
63 $\text{Gd}_{0.24}\text{Fe}_{0.665}\text{Co}_{0.095}$ alloys with time-resolved resonant X-ray scattering. We then compare our
64 data with a multiscale model that utilizes both atomistic and large-scale micromagnetic
65 components to simulate the spatiotemporal evolution of the magnetisation. We identify two
66 distinct dynamic processes we term magnon localisation and magnon coalescence. These
67 processes describe the nucleation and subsequent dynamics of localised textures that arise
68 from attractive nonlinear interactions between thermalized magnons [19]. This is in contrast
69 to theories that predict the order parameter recovery of the spatially averaged magnetisation,
70 as described by the damping of a heated spin-wave distribution [20].

71 Magnon localisation is the process by which small, non-equilibrium, localised magnetic
72 textures nucleate and grow. The textures are necessarily long-term unstable transient features
73 that are not to be confused with magnetic domains, which are equilibrium or meta-stable
74 states. In the context of conservative dynamics, localised textures can be described as
75 dynamical magnon bound states [21] known as magnon drops [22]. Magnon localisation can
76 be detected by the appearance of a broad ring centred at low q in the X-ray scattering pattern
77 with a rapid radius expansion in reciprocal space and simultaneously decreasing ring width.
78 A subsequent shrinking of the ring radius accompanied by the continual decrease in the ring
79 width indicates a stage of magnon drop growth we term magnon coalescence.
80 Microscopically, magnon coalescence is driven by the ongoing nonlinear attraction between
81 magnon drops and unbound magnons that depletes the thermal magnon population as the
82 magnon drops continue to grow, on average. The substantial, highly turbulent flux of angular
83 momentum in the vicinity of magnon drops during the coalescence stage can be estimated by
84 use of numerical simulations that show the presence of strong exchange flow spin currents
85 (EFSCs) [23, 24], which are equivalent to a 100% polarised charge current density on the
86 order of 10^7 A cm^{-2} . These simulation results suggest that magnon drop dynamics driven by
87 such large spin currents expedite magnon coalescence via magnon drop growth, break-up,
88 and merger [25].

89 Our study suggests that the picosecond evolution of the spatially varying magnetisation
90 can be understood from a phase kinetics approach [26, 27]. When the magnetisation
91 quenching upon femtosecond optical pumping is almost 100 %, the initial condition of the
92 system can be described as a non-equilibrium distribution of randomised spins that undergo

93 rapid restoration of the magnetic order parameter, subject to a multiplicity of final
94 equilibrium (or quasi-equilibrium) states. In other words, the subsequent rapid passage from a
95 nearly paramagnetic to a magnetically ordered state will generally do so via pathways of
96 unstable magnon-drop growth, i.e., phase-ordering kinetics. Such dynamics are in contrast to
97 the critical behaviour expected from an adiabatic evolution through a phase transition [28].
98 Because of the large degeneracy of the equilibrium states, unstable growth necessarily leads
99 to pattern formation, examples of which include domains in magnetic materials and metallic
100 alloys [26, 29], phase separation in binary fluids and superfluids [30], and optical solitons
101 [31]. In addition, it has been argued that rapid quenching of a randomised state can
102 dynamically stabilise topological defects via the Kibble-Zurek mechanism [32, 33], as seen in
103 superfluids [30, 34], ferroelectrics [35], magnetic vortices [36], and bubble domain lattices
104 [37]. Therefore, the magnon processes identified here shed light upon the physical
105 mechanisms that are important in the initial stages of unstable growth and pattern formation
106 triggered by ultrafast optical pumping.

107

108 **Results**

109 **X-ray scattering**

110 The evolution of the scattered intensity is measured by time-resolved, resonant magnetic
111 soft X-ray scattering, a pump-probe technique schematically shown in Figure 1 (see details in
112 Methods). A 0.5 T field is applied perpendicular to the film plane during the measurement.
113 As such, the magnetisation is always reset into the saturated state prior to each pump pulse.
114 The element-specific, spatially-averaged dynamics are simultaneously measured by X-ray
115 magnetic circular dichroism (XMCD) of the unscattered beam.

116 From the scattered intensity measurements, we directly obtain the time-varying spin-spin
117 correlation function, $\Delta S^2(q, t)$ (see Methods). This quantity provides information related only
118 to the magnetisation's spatial profile, in contrast to the spin correlations projected onto the
119 sample's chemical nanostructure studied in Ref. [8]. The background spin-spin correlation
120 signal prior to time-zero is an order of magnitude smaller than the features observed at $t > 0$.

121 For illustrative purposes, we show two schematic examples in Figure 2 as to the
122 expected scattering patterns correlated to representative spatial patterns. A broad peak centred
123 at $q = 0$ corresponds to a low density of randomly located textures of variable size [38], as
124 schematically shown in the top row. However, if these azimuthally disordered textures are
125 sufficiently close-packed so as to have a well-defined averaged spatial separation, they will
126 exhibit a long-range correlation length [39], i.e., a ring structure develops, as shown in the
127 bottom row.

128 We measured the magnetisation dynamics for two cases where the XMCD data within
129 20 ps exhibits partial or full quench of the Gd and Fe moments. We refer to non-AOS for
130 partial quench and AOS for full quench. As shown below, the dynamic scattering data are
131 qualitatively similar between these cases. We reiterate that the applied field saturates the
132 sample so that any large amplitude inhomogeneity in the spatial spin distribution is not stable
133 at long times. Non-AOS was obtained with a 30 nm thick sample and an absorbed 800 nm
134 pump fluence of 3.91 mJ cm^{-2} . In Figure 3a, the corresponding XMCD response for both Gd
135 and Fe exhibits a partial quench of the magnetisation for $t < 3 \text{ ps}$, followed by an
136 approximately constant state of demagnetisation up to the longest delay time of 20 ps. AOS
137 was not achieved with the available pump fluences in this sample. Using a 20 nm thick
138 sample and an absorbed 800 nm pump fluence of 4.39 mJ cm^{-2} , AOS was achieved. The

139 XMCD data in this case shows that the magnetic moments are fully quenched and switch at \approx
140 3 ps, as presented in Figure 3b. However, similar to the non-AOS case, the spatially averaged
141 magnetisation remains approximately constant for as long as 20 ps after time-zero. The
142 extremely slow time dependence of the XMCD data in both cases indicates that the average
143 magnetisation is essentially constant for $3 \text{ ps} < t < 20 \text{ ps}$. A critical implication is that the
144 quasi-thermal redistribution of magnon occupation caused by either damping or other
145 inelastic interactions that eventually drives the magnetisation towards a saturated state are not
146 important at these timescales.

147 The azimuthally averaged spin-spin correlation function for Gd in the non-AOS case is
148 shown by contours in Figure 3c. Spin-spin correlation profiles at selected time instances are
149 shown in Figure 3d by solid black curves that have been shifted vertically for clarity. These
150 lineouts have two ring-like spectral features: one with a radius close to or below the smallest
151 resolved wavevectors and one with a radius in the range $0.4 \text{ nm}^{-1} < q < 0.8 \text{ nm}^{-1}$. Fits to the
152 data shown by the dashed red curves are obtained by using a Gaussian line-shape for the
153 high- q feature (with a ring radius indicated by black circles) and a Lorentzian line-shape for
154 the low- q feature. The fitted Gaussian line-shape indicates the appearance of a ring and
155 therefore a short-range correlated magnetisation pattern at sub-picosecond timescales. After \approx
156 5 ps, reliable fits were obtained by use of only a Lorentzian line-shape.

157 For the AOS case, the azimuthally averaged spin-spin correlation shown in Figure 3e
158 exhibits a peak at low q that appears in a fraction of a picosecond. In this measurement, the
159 maximum measured $q \approx 0.46 \text{ nm}^{-1}$ was insufficient to determine the appearance of a Gaussian
160 peak at higher wavevectors. Spin-spin correlation profiles at selected time instances are
161 shown in Figure 3f, with vertically shifted curves for the sake of clarity. Reliable fits were
162 obtained solely by use of a Lorentzian line-shape, shown with the dashed red curves in Figure
163 3f.

164

165 Numerical simulations

166 To understand better the physical mechanisms that are most important in driving
167 spatially inhomogeneous magnetisation dynamics after pumping, we performed atomistic
168 simulations [40, 41]. The amorphous alloy is modelled as a polycrystalline Gd and Fe-Co thin
169 film with elemental inhomogeneity with a characteristic length of 7 nm, guided by recent
170 experimental results [8]. The spatially averaged magnetic moments for Gd and Fe obtained
171 with atomistic simulations are shown in Figure 4a for the non-AOS case utilising an absorbed
172 fluence of 10.7 mJ cm^{-2} and Figure 4b for the AOS case utilising a similar absorbed fluence
173 of 11 mJ cm^{-2} . The atomistic simulations assume uniform heating across the thickness, and
174 the utilised fluences are tuned to qualitatively reproduce the experimental XMCD data, cf. to
175 Figure 3a and b.

176 Snapshots of the simulated perpendicular-to-plane magnetisation evolution are shown in
177 Figure 4c and d for non-AOS and AOS, respectively. In both cases, coarsening of the
178 perpendicular-to-plane magnetisation from a fine-grained randomised state is observed. The
179 similar spatial evolution for both cases suggests that the same dynamic processes take place
180 after ultrafast optical pumping, insofar as the magnetic moments are substantially quenched.
181 The coarsening of the spatially varying magnetisation at such short time-scales is necessarily
182 the result of spin-conserving nonlinear magnon interactions, whereby spatial localisation of
183 textures rapidly minimizes magnon energy [21, 22] while maintaining a quenched, average
184 magnetisation. This is in contrast to the simple picture of field-driven growth of domains in

185 an applied field that is operative on much longer timescales, on the order of hundreds of
186 picoseconds [42].

187 To directly compare with the experimental results, the simulated spin-spin correlation
188 function is calculated via Fourier analysis of the spatially-dependent perpendicular-to-plane
189 magnetisation. Contours of the azimuthally averaged spin-spin correlation function in the
190 non-AOS case are shown in Figure 5a. Lineouts at selected time instances are shown in
191 Figure 5b in addition to fits of the relevant diffraction rings by a linear combination of
192 Lorentzian and Gaussian functions centred at $q > 0$ with radius positions indicated by black
193 circles. While the appearance of the Gaussian peak is less apparent than in the case for the
194 data in Figure 3d, the precise fitting of the ring radius and width was still possible, as we
195 further demonstrate below. For the case of AOS, contours of the azimuthally averaged spin-
196 spin correlation function are shown in Figure 5c while selected lineouts and Lorentzian fits
197 are shown in Figure 5d by solid black and dashed red curves, respectively. Both cases
198 qualitative agree with the experimental data.

199 To further identify the role of exchange coupling between the rare earth (Gd) and
200 transition metal (Fe) lattices, we performed multiscale micromagnetic simulations based on
201 the Landau-Lifshitz (LL) equation [43] that consider an effective, homogeneous exchange
202 stiffness, see Supplementary Note 1. The ferrimagnetic GdFeCo is modelled as a single-
203 species ferromagnet, with an initial condition provided by the atomistic simulations at a
204 specified delay $t_c \geq 3$ ps after optical pumping. By use of this multiscale approach, we can
205 isolate the role of the atomic-scale exchange interactions, which dominate at short times,
206 from the longer-range exchange stiffness. Because the micromagnetic model approximates
207 exchange dispersion as q^2 , spatial fluctuations should be sufficiently concentrated on small
208 wavenumbers. However, the choice of t_c within 10 ps does not significantly change the
209 qualitative features of the magnetisation's coarsening (see Supplementary Note 2). As such,
210 we only show a representative example at the shortest delay, $t_c = 3$ ps, at the limit of the
211 micromagnetic approximation.

212 For micromagnetic simulations in the non-AOS case, the azimuthally averaged spin-spin
213 correlation function is shown in Figure 5e. The black area indicates the temporal range in
214 which atomistic simulations are used to calculate the initial conditions for the micromagnetic
215 simulations. Corresponding lineouts, along with fits by the previously described sum of
216 Lorentzian and Gaussian functions, are shown in Figure 5f by solid black and dashed red
217 curves, respectively. A striking feature is that the Gaussian profile diffraction ring, identified
218 by black circles, persists as long as 10 ps, suggesting slower dynamics are at play in the
219 micromagnetic approximation. After 10 ps, fits of the low- q diffraction ring with a
220 Lorentzian function break down. Better fits are achieved by use of a squared Lorentzian
221 function that exhibits a q^{-4} -like decay. This is an artefact associated with the approximation
222 that the magnetisation in each cell is uniform, with sharp magnetic interfaces between cells.
223 Such a form factor is an artificial constraint in the finite-difference micromagnetic
224 simulations which is avoided in atomistic simulations. For the case of AOS, the azimuthally
225 averaged spin-spin correlation function is shown in Figure 5g. Lineouts and corresponding
226 squared Lorentzian fits are shown in Figure 5h. The qualitative agreement to both
227 experimental data and atomistic simulations suggests that atomic-scale exchange interactions
228 have a limited influence on the dynamics when only a single line-shape can be fitted.

229

230

231

232 **Imprinted demagnetisation and dissociation**

233 The high- q diffraction ring in the non-AOS case appears during the optically-induced
234 quench of the magnetic moments, indicating short-range correlations. To conclusively
235 elucidate the physical mechanisms that drive the magnetisation dynamics at such short
236 timescales, we analyse the fitted parameters obtained from experiments and atomistic
237 simulations. The fitted Gaussian line-shape with ring radius q_{\max} , ring width σ_q , and
238 normalized ring amplitude are shown in Figure 6a, b, and c, respectively. Fits to the
239 experimental data are shown in the Supplementary Note 3.

240 The blue circles are obtained from fits to experiments. For the first ≈ 3 ps, the XMCD
241 data in Figure 3a indicates that the spatially averaged Gd magnetisation is 75 % quenched. At
242 the same time, both the ring radius and the ring width are approximately constant at $q_{\max} =$
243 $0.57 \pm 0.014 \text{ nm}^{-1}$ and $\sigma_q = 0.24 \pm 0.002 \text{ nm}^{-1}$, though the ring amplitude continues to
244 increase. The ring radius is consistent with a magnetisation pattern of a 11 nm characteristic
245 correlation length, similar to the ≈ 10 nm average chemical inhomogeneity characteristic of
246 such amorphous GdFeCo alloys [8]. Fits to atomistic simulations shown by the red circles in
247 Figure 6 exhibit a similar behaviour. For the simulated fluence, the demagnetisation is almost
248 100 % by 2 ps, at which point the average fitted ring radius and ring width are $q_{\max} = 0.88 \pm$
249 0.012 nm^{-1} and $\sigma_q = 0.18 \pm 0.04 \text{ nm}^{-1}$, respectively. The corresponding correlation length of
250 7.1 nm agrees well with the chemical correlation length used for the simulation. The
251 diffraction ring amplitude also increases with time for the first 2 ps during the fastest part of
252 the demagnetisation.

253 Both experiments and simulations provide evidence for an optically-induced spatial
254 demagnetisation pattern that imprints on the material's chemical inhomogeneities. The short
255 spatial fluctuations require an atomistic description. This imprinted demagnetisation is
256 supported by the previously identified sub-ps transfer of angular momentum between
257 chemical species [8].

258 Between ≈ 3 ps and ≈ 4.5 ps the fitted ring radius from experiments shifts towards lower
259 q . Unlike the experimental data, the high- q diffraction ring amplitude from atomistic
260 simulations collapses after 3 ps, making further comparison between experiments and
261 simulations impossible. Regardless, the shift in the ring radius for both data and simulations
262 indicates that the magnetic system dissociates from the sample's chemical inhomogeneity,
263 and transitions into a state where any correlations are emergent features of the magnetisation
264 energetics itself. We interpret these features as a collection of randomly located localised spin
265 textures. Such a rapid dissociation is facilitated by the nonlinear attraction of high energy
266 magnons to each other [21]. This effect is a consequence of the focusing nature of the
267 effective nonlinear anisotropy and is well-known in other nonlinear systems such as
268 photonics [44, 45] and Bose-Einstein condensates [46]. For this reason, we generically refer
269 to the resulting localised textures as magnon drops [22].

270 In the case of AOS, we surmise that a similar imprinted demagnetisation and subsequent
271 dissociation processes must occur at short time scales, as suggested in Ref. [8], although our
272 experimental data was not collected at the relevant wavevectors and atomistic simulations did
273 not exhibit strong enough features to be reliably fitted.

274

275

276

277 **Magnon localisation and coalescence**

278 The subsequent evolution of the magnetisation is quantified from the Lorentzian fits to
279 the low- q diffraction ring. Details of the fitting procedure are discussed in the Supplementary
280 Note 4. The two fitted quantities of interest are the ring radius and the ring width. These
281 quantities provide information on the size of and spatial spacing between magnon drops. A
282 collection of randomly located magnon drops, regardless of their spatial spacing, constitute
283 random telegraph noise that results in a Lorentzian line-shape centred at $q = 0$ whose ring
284 width is inversely proportional to the average magnon drop size. However, because
285 overlapping magnon drops compose a single feature, a finite ring radius inversely
286 proportional to the magnon drops' spatial spacing ensues. These spectral features are similar
287 to those observed in X-ray scattering experiments of a molecular liquid-liquid transition
288 where hard-core-like repulsive interactions between so-called locally favoured structures is
289 invoked [47].

290 The absence of harmonics indicates that the magnon drops' size distribution dominates
291 the scattering: a periodic array of identically sized magnon drops would consist of harmonic
292 rings by virtue of a Fourier series decomposition whose harmonic-dependent coefficients
293 would encode the magnon drops' size and profile. Deviations of the lattice periodicity would
294 result only in the rings' spectral broadening.

295 The evolution of the fitted ring radius is shown in Figure 7a and b for non-AOS and
296 AOS cases, respectively. The evolution of the average magnon drop diameter $L = 2\pi / \Delta q$,
297 where Δq is the ring width, is shown in Figure 7c and d for non-AOS and AOS cases. Blue,
298 red, and black circles correspond to, respectively, experiments, atomistic simulations, and
299 micromagnetic simulations.

300 In the experimental non-AOS case, a ring with a non-zero radius appears after 5 ps. The
301 ring radius increases for the first 3 ps, indicating that the average spatial spacing is decreasing
302 as magnon drops continue to nucleate. A maximum ring radius of $0.0626 \text{ nm}^{-1} \pm 0.0011 \text{ nm}^{-1}$
303 is observed at 8 ps, corresponding to an average spatial spacing of $\approx 100 \text{ nm} \pm 11 \text{ nm}$. During
304 the same temporal window, the average magnon drop diameter increases from ≈ 10 to ≈ 20
305 nm. The observation of an expanding ring radius accompanied by the growth of magnon drop
306 diameters defines the magnon localisation process. During this stage, an initially sparse
307 collection of magnon drops becomes close-packed because of the continual nucleation of
308 magnon drops.

309 At longer times, the ring radius drops and appears to reach a plateau at $0.0334 \text{ nm}^{-1} \pm$
310 0.0016 nm^{-1} that corresponds to an average spacing of $\approx 188 \text{ nm} \pm 9 \text{ nm}$. However, L
311 continues to increase approximately following a power law growth. This behaviour is
312 consistent with the growth of the already present magnon drops via merger and break-up as
313 well as nonlinear attraction of thermal magnons, so that the average spatial spacing increases.
314 We refer to this dynamical process as magnon coalescence and is characterised by the
315 shrinking of the scattered ring radius and width.

316 The fits to the atomistic data in the non-AOS case return a qualitatively similar
317 behaviour for both the ring radius and L . Micromagnetic simulations exhibit delayed
318 development of the low- q diffraction ring, with an onset of a non-zero ring radius at ≈ 10 ps.
319 Such delayed dynamics result from the micromagnetic magnon dispersion proportional to q^2 ,
320 an approximation that is only valid at long wavelengths, as opposed to the more accurate $1 -$
321 $\cos(qa)$ form associated with quantum mechanical exchange in a periodic lattice with lattice
322 constant a . Consequently, upon transference of the spatial magnetisation distribution from the
323 atomistic to the micromagnetic simulations, magnons with wavenumbers approaching the

324 Brillouin zone boundary convey an artificially inflated amount of thermal energy into the
325 spin system. This artificially inflated spin temperature commensurately increases the time
326 required to form magnon drops of a similar size to those obtained via the more accurate
327 atomistic simulations. Despite this caveat, the qualitative features of the low- q ring obtained
328 micromagnetically agree with the occurrence of magnon localisation and magnon
329 coalescence.

330 For the AOS case, Figure 7b, the low- q ring radius for the experimental data is non-zero
331 after ≈ 2.5 ps. The ring radius monotonically increases to a maximum of $\approx 0.047 \text{ nm}^{-1} \pm$
332 0.001 nm^{-1} at the longest experimental delay time of 20 ps, corresponding to a minimum
333 average spacing of $\approx 133 \text{ nm} \pm 2 \text{ nm}$. The associated evolution of L , Figure 7d, exhibit a
334 fixed value of $\approx 100 \text{ nm}$ for ≈ 7 ps, after which L gradually increases to 250 nm out to the
335 longest delay times. Viewed together with the evolution of the average spatial spacing, the
336 process of AOS appears to be one in which switching is mediated by an ever decreasing
337 spacing between drops, due to monotonically increasing density of magnon drops. In other
338 words, only magnon localisation is operative for AOS, in a manner consistent with the
339 eventual switching of the macroscopic magnetisation. This is in clear contrast to the case of
340 non-AOS, where the magnon localisation is arrested and gives way to magnon coalescence.

341 Atomistic simulations in the AOS case yield a much more rapid increase in the ring
342 radius on a time scale of 4 ps, followed by a slow reduction until the radius is close to that of
343 the experimental data at the longest delay. Micromagnetic simulations exhibit a similar
344 increase in the ring radius between 4 and 10 ps, at which point the maximum ring radius is
345 0.09 nm^{-1} . However, there is a rapid collapse of the ring radius after 10 ps, such that the
346 spatial spacing completely diverges at 11 ps. The failure of both the atomistic and
347 micromagnetic models to quantitatively reproduce the evolution of the ring radius in the AOS
348 case suggests that there remains important non-equilibrium physics that affect the rapid
349 magnetisation dynamics in amorphous alloys, which are not contained in either our atomistic
350 or micromagnetic simulations.

351 Despite differences in ring radii for both AOS and non-AOS, the similar monotonic
352 increase of L for both experiments and simulations with time after 4 ps, indicates that the
353 necessary physics to describe the growth of magnon drops at ps time scales are properly
354 captured by the models. More importantly, the fact that micromagnetic simulations can
355 qualitatively describe the evolution of L beyond 10 ps indicates that nothing more than
356 exchange stiffness and uniaxial anisotropy are necessary to drive the growth of magnon
357 drops.

358 Power law fits to L are shown in Figure 7c and d by colour coded dashed lines that
359 utilise the fitting function $L(t) = bt^a$. The resultant fitting parameters are listed in Table 1.
360 We find exponents in the range $0.71 \leq a \leq 1.14$ for all cases. Fits to experimental data
361 obtained at different fluences for both Gd and Fe yield exponents of similar values (see
362 Supplementary Note 5). Taking into account exponents obtained from experiments and
363 simulations, we obtain an average exponent of $a = 0.82 \pm 0.04$.

364 Domain growth in 2nd order phase kinetics in a non-conservative system is typically
365 modelled with Lifshitz-Cahn-Allen (LCA) theory, which postulates that domain wall velocity
366 is linearly proportional to the local curvature of the phase interface. This leads to power-law
367 growth of phase-ordered domains with an exponent of 1/2 [26, 48, 49], confirmed in 2D
368 simulations, e.g. Refs. [50] and [51]. Solid magenta lines in Figure 7c and d show exemplary
369 LCA behaviour. However, LCA assumes domain growth proceeds by progression through a
370 continuous series of intermediate, energetically favoured meta-stable states via short-range

371 interactions. As such, the applicability of LCA is questionable in the case of magnon drops,
372 where spins at the magnon drop perimeter are necessarily dynamic, and where long-range
373 spin interactions can be mediated by both nonlocal dipole fields [29] and the hydrodynamic
374 flow of angular momentum via exchange [23, 24, 52, 53], all of which would tend to
375 decouple the domain growth rate from the phase boundary local curvature.

376

377 **Magnon drop dynamics via exchange flows of spin current**

378 Analysis of the magnetisation dynamics from a micromagnetic perspective can shed
379 light onto the origins of how L grows during magnon coalescence. Interactions between
380 magnon drops can be quantified and visualized in terms of the long-range transmission of
381 angular momentum arising from the noncollinear magnetisation [54]. Utilising a
382 hydrodynamic representation [23, 24, 52, 53], the transfer of angular momentum is
383 represented by exchange flow spin currents (EFSCs). EFSCs can be expressed as an
384 equivalent charge current density that is 100% polarised in the perpendicular-to-plane
385 direction [23, 24].

386 Examples of EFSCs mediating magnon drop interactions in micromagnetic simulations
387 are shown in Figure 8 by three snapshots spanning a 2 ps time interval. The magnon drops'
388 perimeters, where the perpendicular-to-plane magnetisation is less than 0.2, are represented
389 as solid black areas. The white and grey background indicate areas where the perpendicular-
390 to-plane magnetisation is preferentially parallel ($m_z > 0.2$) or anti-parallel ($m_z < 0.2$) to the
391 applied field. The grey areas are nascent magnon drops in the early evolution of the phase
392 coarsening process. The pink-shaded streamlines represent the flow of angular momentum
393 quantified by EFSCs. We find that spin currents with an equivalent charge current density on
394 the order of 10^7 A cm⁻² can persist for many 10's of ps after optical pumping. Such
395 magnitudes are similar to those used for magnetisation switching via spin transfer torque
396 [55]. While the EFSCs are spatially nonuniform and highly turbulent, they can effectively
397 deform the magnon drops' perimeters, causing drops to both breathe and rotate [56].
398 Furthermore, the EFSCs mediate long-range interactions between magnon drops that result in
399 both mergers and break-ups [25]. An example of a merger is observed between the leftmost
400 and central magnon drops, labelled A and B, respectively. At 25 ps, large-magnitude EFSCs
401 flow between the magnon drops, so that a torque is exerted at the perimeters. At 26 ps and 27
402 ps, the perimeters merge into a single drop B and continue to transfer angular momentum.
403 Examples of break-up are observed at the top of the central magnon drop, where EFSCs
404 transfer angular momentum away from the magnon drop. As a result, the top-left and top
405 magnon drops, labelled C and D, break up at 26 ps and 27 ps, respectively.

406

407 **Discussion**

408 While our experimental and numerical results focus on the first 20 ps evolution of the
409 magnetisation in GdFeCo alloys, these dynamics shed light onto the nonlinear magnon
410 processes that drive coarsening while the spin system equilibrates.

411 The qualitative agreement between experiments and multiscale simulations demonstrates
412 that current models incorporate the most important physical effects responsible for the
413 nonlinear magnon processes identified here. From a theoretical perspective, this agreement
414 implies that appropriate scaling of the equation of motion can be used to describe other
415 magnetic materials insofar as they exhibit perpendicular magnetic anisotropy and a net

416 magnetisation at equilibrium. In other words, the magnon processes described here are
417 universal for PMA ferromagnets and ferrimagnets. To substantiate this claim, we performed
418 additional atomistic simulations for a chemically homogeneous GdFeCo (see Supplementary
419 Note 6). The evolution of the spatially varying magnetisation is consistent with a magnon
420 coalescence process at times greater than 5 ps. Because there are no inhomogeneities to seed
421 a magnetisation pattern during demagnetisation, we conclude that magnon localisation and
422 coalescence in PMA magnets are indeed general processes that are independent of the
423 material's structure, although the details of the spatial evolution process can be affected by
424 the presence of chemical inhomogeneities. In addition, micromagnetic simulations in the
425 magnon coalescence regime exhibit qualitatively similar evolution of both the ring radius and
426 the average magnon drop diameter L for different sample thicknesses, initial state of spatial
427 magnetisation, and variation of other micromagnetic parameters (see Supplementary Note 7).

428 From a theoretical point of view, the hydrodynamic formulation of magnetisation
429 dynamics provides a valuable tool to understand the long-time magnetisation evolution. For
430 example, the nucleation of topological defects after fast quench [36, 37] represents an
431 interesting possibility in the context of optically-induced applications. In the hydrodynamic
432 formulation, topological defects are evidenced by curved trajectories in the EFSCs [23].
433 However, an accurate calculation of the topological number for a spatially localised defect
434 requires a uniform magnetisation surrounding the defect [57]. In other words, defects must be
435 sparsely located. We surmise that understanding the evolution of EFSCs from tens to
436 hundreds of picoseconds timescales, where dissipative processes are operable, will lead to a
437 better understanding of the dynamic evolution of topological defects upon ultrafast optical
438 pumping.

439 Based on our study, we speculate that desired magnetisation states may be stabilised by
440 nanopatterning magnetic materials to take advantage of both sub-picosecond seeded
441 magnetisation states and EFSCs, even for crystalline materials. For example, a close-packed
442 spatially periodic patterning may favour a like-wise close-packed magnetisation pattern
443 during localisation to induce AOS. Conversely, sparse engineered defects may serve as
444 pinning potentials to stabilise topological defects.

445

446 **Methods**

447 Experiments

448 The GdFeCo samples were fabricated on 100 nm thick Si₃N₄ membranes by magnetron
449 sputtering. A 5 nm seed layer of Si₃N₄ was first grown on the membrane followed by the
450 Gd_{0.24}Fe_{0.665}Co_{0.095} film, which was then capped with 20 nm of Si₃N₄. X-ray measurements
451 were conducted at the SXR hutch of the Linac Coherent Light Source [58]. The X-ray energy
452 was selected to be resonant with the Fe L₃ resonance edge at 707 eV or the Gd M₅ resonance
453 edge at 1185 eV with a 0.5 eV bandwidth and a pulse duration of 80 fs. The X-ray pulses
454 were circularly polarised at the Fe L₃ and Gd M₅ edges by using the XMCD in magnetized Fe
455 and GdFe films respectively placed upstream of the experiment. A degree of polarization was
456 85% at the Fe L₃ edge and 79% at the Gd M₅ edge. Measurements were made in transmission
457 geometry with X-rays incident along the sample normal. An in-vacuum electromagnet was
458 used to apply a field of 0.5 T perpendicular to the GdFeCo film. The diffracted X-rays were
459 collected with a p-n charge-coupled device (pnCCD) two-dimensional detector placed behind
460 the sample. A hole in the centre of the detector allowed the transmitted beam to propagate to
461 a second detector used to collect the transmitted X-ray beam. The experiment was conducted
462 in an optical pump – X-ray probe geometry. Optical pulses of 1.55 eV and 50 fs duration

463 were incident on the sample in a near collinear geometry. The delay between the optical and
 464 X-ray pulses was achieved using a mechanical delay line, where the delay was continuously
 465 varied. X-ray–optical jitter was monitored and removed from the experimental data using an
 466 upstream cross-correlation arrival monitor [59].

467

468 Atomistic simulations

469 A model system of a GdFe ferrimagnet was developed to perform numerical simulations of
 470 the atomistic spin dynamics after femtosecond laser excitation. The inhomogeneous
 471 microstructure is generated by specifying random seed points representing areas of
 472 segregation of the Gd from the alloy, leading to 15% to 30% higher local Gd concentration.
 473 These regions are interpolated using a Gaussian with a standard deviation of 5 nm,
 474 representing the scale of the segregation. Due to low packing of the seed points, the
 475 characteristic length of the spatial variations is approximately 7 nm. An atomistic level
 476 simulation model is used to properly describe the ferrimagnetic ordering of the atomic
 477 moments with Heisenberg exchange [40]. The energy of the system is described by the spin
 478 Hamiltonian

$$479 \quad \mathcal{H} = -\sum_{i<j} J_{ij} \mathbf{S}_i \cdot \mathbf{S}_j - \sum_i k_u (S_i^z)^2, \quad (1)$$

480 where the spin \mathbf{S}_i is a unit vector describing the local spin direction. J_{ij} is the exchange
 481 integral, which we limit to nearest neighbour interactions, and k_u is the anisotropy constant.
 482 Time-dependent spin dynamics are governed by the Landau-Lifshitz-Gilbert (LLG) equation
 483 at the atomistic level

$$484 \quad \partial_t \mathbf{S}_i = -\frac{\gamma}{(1+\alpha^2)} [\mathbf{S}_i \times \mathbf{B}_{\text{eff}}^i + \alpha \mathbf{S}_i \times (\mathbf{S}_i \times \mathbf{B}_{\text{eff}}^i)], \quad (2)$$

485 where γ is the gyromagnetic ratio and $\alpha = 0.01$ is the Gilbert damping factor. The on-site
 486 effective induction can be derived from the spin Hamiltonian with the local field augmented
 487 by a random field to model the interactions between the spin and the heat bath

$$488 \quad \mathbf{B}_{\text{eff}}^i = -\frac{1}{\mu_i} \frac{\partial \mathcal{H}}{\partial \mathbf{S}_i} + \zeta_i, \quad (3)$$

489 where the second term ζ_i is a stochastic thermal field due to the interaction of the conduction
 490 electrons with the local spins, and μ_i is the local (atomic) spin magnetic moment. The
 491 stochastic thermal field is assumed to have Gaussian statistics and satisfies

$$492 \quad \langle \zeta_{i,a}(t) \zeta_{j,b}(t') \rangle = \delta_{ij} \delta_{ab} (t - t') 2\alpha_i k_B T_e \mu_i / \gamma_i, \quad (4)$$

$$493 \quad \langle \zeta_{i,a}(t) \rangle = 0, \quad (5)$$

494 where k_B is the Boltzmann constant and T is the temperature. We incorporate the rapid
 495 change in thermal energy of a system under the influence of a femtosecond laser pulse. The
 496 spin system is coupled to the electron temperature, T_e , which is calculated using the two-
 497 temperature model [60] with the free electron approximation for the electrons

$$498 \quad T_e C_e \frac{dT_e}{dt} = -G_{\text{el}}(T_l - T_e) + P(t), \quad (6)$$

$$499 \quad C_l \frac{dT_l}{dt} = -G_{\text{el}}(T_e - T_l), \quad (7)$$

500 where $C_e = 225 \text{ J m}^{-3} \text{ K}^{-1}$, $C_l = 3.1 \times 10^6 \text{ J m}^{-3} \text{ K}^{-1}$, $G_{\text{el}} = 2.5 \times 10^{17} \text{ W m}^{-3} \text{ K}^{-1}$, and $P(t)$
 501 models the temperature from a single Gaussian pulse into the electronic system. The pulse
 502 has a width of 50 fs.

503 We use Heun numerical integration scheme to integrate the stochastic equation of motion
 504 with time-varying temperature [41]. We use $\mu_{\text{Fe}} = 1.92\mu_{\text{B}}$ as an effective magnetic moment
 505 containing the contribution of Fe and Co and we set $\mu_{\text{Gd}} = 7.63\mu_{\text{B}}$ for the Gd sites, where μ_{B}
 506 is Bohr's magneton. The standard parameters of the exchange coupling constants are used:
 507 $J_{\text{Fe-Fe}} = 4.526 \times 10^{-21} \text{ J per link}$, $J_{\text{Gd-Gd}} = 1.26 \times 10^{-21} \text{ J per link}$, and $J_{\text{Fe-Gd}} = -1.09 \times$
 508 $10^{-21} \text{ J per link}$. We assume a uniaxial anisotropy energy of $8.07246 \times 10^{-24} \text{ J per atom}$.
 509 The numerical simulations are conducted using the VAMPIRE software package [41]. The
 510 simulation volumes were $200 \text{ nm} \times 200 \text{ nm} \times 2 \text{ nm}$ and $1000 \text{ nm} \times 1000 \text{ nm} \times 2 \text{ nm}$.

511

512 Multiscale micromagnetic simulations

513 Micromagnetic simulations were performed with the graphic processing unit (GPU) package
 514 MuMax3 [61] that solves the Landau-Lifshitz equation for a ferromagnet

$$515 \quad \partial_t \mathbf{m} = -\gamma \mu_0 [\mathbf{m} \times \mathbf{B}_{\text{eff}} + \alpha \mathbf{m} \times \partial_t \mathbf{m} \times \mathbf{B}_{\text{eff}}], \quad (8)$$

516 where μ_0 is the vacuum permeability, \mathbf{m} is the magnetisation vector normalised to the
 517 saturation magnetisation, and \mathbf{B}_{eff} is an effective induction that includes the required physical
 518 terms to model a ferromagnetic material. Here, we included exchange, nonlocal dipole,
 519 uniaxial anisotropy, and external fields. The exchange interaction in the micromagnetic
 520 approximation takes the form of a Laplacian scaled by the exchange length, λ_{ex} . In MuMax3,
 521 the Laplacian is numerically resolved by a 4th order central finite difference scheme, i.e., each
 522 micromagnetic cell is subject to exchange interaction due to itself and two neighbouring cells
 523 in each dimension. We ran our simulations on NVIDIA GPU units K20M, K40, K80, and
 524 P100. Due to the coarse resolution of micromagnetic simulations, we utilise approximately
 525 cubic cells of size $2 \text{ nm} \times 2 \text{ nm} \times \delta$, where $\delta = D/2^N$ and the factor N is chosen to take
 526 advantage of the GPU spectral calculations such that $\delta < \lambda_{\text{ex}} \approx 5 \text{ nm}$ and D is the physical
 527 thicknesses equal to 30 nm or 20 nm for the non-AOS or AOS cases, respectively. The lateral
 528 simulation area was determined from atomistic simulations and the full thickness for each
 529 case was achieved upon the atomistic observation that the magnetisation is approximately
 530 homogeneous across the thickness at $t \geq 3 \text{ ps}$. The coarse micromagnetic discretization allows
 531 for a significant speed up in the computations. Note that the size of the cells only impacts the
 532 stability and accuracy of the numerical algorithm while the physics can only be interpreted in
 533 the framework of the continuum Landau-Lifshitz equation, i.e., long-wavelength features
 534 relative to the exchange length. We set the software to solve equation (8) with an adaptive-
 535 step, 4th order Runge-Kutta time integration method. Periodic boundary conditions (PBCs)
 536 were imposed along the film's plane. For both dynamical behaviours we used the equilibrium
 537 magnetic parameters: saturation magnetisation $M_{\text{S}} = 47170.6 \text{ A m}^{-1}$, anisotropy constant $k_{\text{u}} =$
 538 $31127.228 \text{ J m}^{-2}$, exchange constant $A = 1 \text{ pJ m}^{-1}$, and $\alpha = 0.01$. The value for A was
 539 numerically found to best match the atomistic, average perpendicular magnetisation evolution
 540 (See Supplementary Note 1).

541

542

543

544 Change in the spin-spin correlation function

545 Experimentally, the change in the spin-spin correlation function, $\Delta S^2(q, t)$, was obtained from
 546 the scattered intensities of circularly polarised X-rays. For this, the scattering intensities are
 547 added to obtain

$$548 \quad S^2(q, t) + C^2(q) = \frac{I_+(q, t) + I_-(q, t)}{2}, \quad (9)$$

549 where $I_+(q, t)$ and $I_-(q, t)$ are the time-dependent scattered intensities obtained with right-
 550 handed and left-handed circularly polarised light, $S^2(q, t)$ is the spin contribution to the
 551 intensity, and $C^2(q)$ is the charge contribution to the intensity. Because the charge
 552 contribution is time-independent for the used pump fluences, the spin-spin correlation
 553 function can be isolated as

$$554 \quad \Delta S^2(q, t) = S^2(q, t) - \mathbb{E}[S^2(q, t < 0)], \quad (10)$$

555 where the background was subtracted by averaging the data collected at times before the
 556 optical pulse irradiated the sample.

557 To compare the data with simulations, the spin-spin correlation function for both atomistic
 558 and micromagnetic simulations was determined by computing a two-dimensional fast Fourier
 559 transform (FFT) of the perpendicular magnetisation for each layer as a function of time. To
 560 minimise error, the FFTs obtained for each layer at a given time were averaged. Since
 561 periodic boundary conditions were used for simulations, a window function was not
 562 necessary.

563

564 Exchange flow spin currents

565 In the dispersive hydrodynamic formulation of magnetisation dynamics [23, 24], the
 566 normalised magnetisation vector $\mathbf{m} = (m_x, m_y, m_z)$ in equation (8) can be cast in
 567 hydrodynamic variables by the canonical transformation

$$568 \quad n = m_z, \quad \mathbf{u} = -\nabla \arctan[m_y/m_x], \quad (11)$$

569 where n is the spin density and \mathbf{u} is the fluid velocity. For the case of conservative dynamics,
 570 $\alpha = 0$ in equation (8), the dispersive hydrodynamic equations are

$$571 \quad \partial_t n = \nabla \cdot [(1 - n^2)\mathbf{u}], \quad (12)$$

$$572 \quad \partial_t \mathbf{u} = -\nabla[(1 - |\mathbf{u}|^2)n] - \nabla \left[\frac{\Delta n}{1 - n^2} + \frac{n|\nabla n|^2}{(1 - n^2)^2} \right] - \nabla h_0, \quad (13)$$

573 expressed in dimensionless space, time, and field scaled by, respectively $\sqrt{|H_k/M_S - 1|}\lambda_{\text{ex}}^{-1}$,
 574 $\gamma\mu_0|H_k - M_S|$, and M_S^{-1} , where the anisotropy field is given by $H_k = 2k_u/(\mu_0 M_S)$, and h_0 is
 575 a dimensionless field applied normal to the plane. The spin density flux in equation (13) is
 576 identified as the EFSC in hydrodynamic variables. To establish a clear comparison to spin
 577 currents obtained by charge-to-spin transduction, the EFSC are expressed as a 100% spin
 578 polarised charge current density in units of A m^{-2} by [24]

$$579 \quad \mathbf{J}_S = -\frac{2e}{\hbar}\mu_0 M_S^2 \lambda_{\text{ex}} \left(\frac{H_k}{M_S} - 1 \right)^{-1/2} (1 - n^2)\mathbf{u}. \quad (14)$$

580 We note that the factor $(1 - n^2)$ leads to maximum EFSC for a given \mathbf{u} when the
581 magnetisation is in the plane. For this reason, the magnon drop perimeters are primarily
582 subject to EFSCs.

583

584 **Data availability**

585 The data that supports the findings of this study are available from the corresponding author
586 upon reasonable request.

587

588 **Code availability**

589 MUMAX³ is open source software and available from <http://mumax.github.io>. VAMPIRE 5 is open source
590 software and available from <https://vampire.york.ac.uk>. The data fitting procedure and calculation
591 of EFSC were custom written in MATLAB and are available from the corresponding and
592 leading author upon reasonable request.

593

594 **Acknowledgements**

595 This material is based upon work supported by the U.S. Department of Energy, Office of
596 Science, Office of Basic Energy Sciences under Award Number 0000231415 and is partly
597 supported by the European Research Council ERC Grant agreement No. 339813 (Exchange)
598 and the Netherlands Organisation for Scientific Research (NWO). Operation of LCLS is
599 supported by the U.S. Department of Energy, Office of Basic Energy Sciences under contract
600 No. DE-AC02-76SF00515. The atomistic simulations in this work used the ARCHER UK
601 National Supercomputing Service (<http://www.archer.ac.uk>) and used code enhancements
602 implemented and funded under the ARCHER embedded CSE programme (eCSE0709). This
603 project has received funding from the European Union's Horizon 2020 research
604 and innovation programme under grant agreement No. 737093 (FEMTOTERABYTE). This
605 work was performed using resources provided by the Cambridge Service for Data Driven
606 Discovery (CSD3) operated by the University of Cambridge Research Computing Service
607 (<http://www.csd3.cam.ac.uk/>), provided by Dell EMC and Intel using Tier-2 funding from the
608 Engineering and Physical Sciences Research Council (capital grant EP/P020259/1), and
609 DiRAC funding from the Science and Technology Facilities Council (www.dirac.ac.uk). E.I.
610 acknowledges support from the Swedish Research Council, Reg. No. 637-2014-6863.
611 M.A.H. was partially supported by NSF CAREER DMS-1255422. L.L.G. would like to
612 thank the VolkswagenStiftung for the financial support through the Peter-Paul-Ewald
613 Fellowship. R.W.C. is grateful to Radboud University, Nijmegen, for hospitality under the
614 Radboud excellence scheme. E.I. thanks Leo Radzihovsky for fruitful discussions.

615

616 **Author contributions**

617 E.I. performed micromagnetic simulations. A.T. prepared the samples. A.H.R., T.-M.L.,
618 P.W.G., E.J., A.X.G., S.B., C.E.G., R.K., Z.C., D.J.H., T.C., L.L.G., K.H., H.O., W.F.S.,
619 G.L.D., G.C., M.C.H., S.C., A.K., A.V.K., T.R., J.S., and H.A.D. performed experiments.
620 Z.F. and R.F.L.E. performed atomistic simulations. R.F.L.E. developed the numerical
621 representation of Fe and Gd inhomogeneities in the atomistic model. Z.F., S.R., R.F.L.E.,

622 T.O. and R.W.C. analysed the atomistic data. T.-M.L. and D.J.H. analysed the experimental
623 data. E.I., M.A.H., and T.J.S. fitted the data and analysed the micromagnetic simulations. All
624 authors contributed to discussions, data analysis, and writing the manuscript.

625

626 **Data availability**

627 The data that supports the findings of this study are available from the corresponding author
628 upon reasonable request.

629

630 **Competing financial interests**

631 The authors declare no competing financial interests.

632

633 **Competing interests**

634 One of the authors, K.H., is an editor on the staff of Nature Communications, but was not in
635 any way involved in the journal review process.

636

637 References

- 638 [1] E. Beaurepaire, J.-C. Merle, A. Daunois, and J.-Y. Bigot, Ultrafast Spin Dynamics in
639 Ferromagnetic Nickel, *Phys. Rev. Lett.* **76**, 4250 (1996)
- 640 [2] C. D. Stanciu, F. Hansteen, A. V. Kimel, A. Kirilyuk, A. Tsukamoto, A. Itoh, and Th.
641 Rasing, All-Optical Magnetic Recording with Circularly Polarized Light, *Phys. Rev. Lett.* **99**,
642 047601 (2007)
- 643 [3] G. Malinowski, F. D. Longa, J. H. H. Rietjens, P. V. Paluskar, R. Huijink, H. J. M.
644 Swagten, and B. Koopmans, Control of Speed and Efficiency of Ultrafast Demagnetisation
645 by Direct Transfer of Spin Angular Momentum, *Nature Phys.* **4**, 855-858 (2008)
- 646 [4] I. Radu et al., Transient Ferromagnetic-like State Mediating Ultrafast Reversal of
647 Antiferromagnetically Coupled Spins, *Nature* **472**, 205-208 (2011)
- 648 [5] B. Vodungbo et al., Laser-Induced Ultrafast Demagnetisation in the Presence of a
649 Nanoscale Magnetic Domain Network, *Nature Comm.* **3**, 999 (2012)
- 650 [6] B. Pfau et al., Ultrafast Optical Demagnetisation Manipulates Nanoscale Spin Structure
651 in Domain Walls, *Nature Comm.* **3**, 110 (2012)
- 652 [7] T. A. Ostler et al., Ultrafast Heating as Sufficient Stimulus for Magnetisation Reversal in
653 a Ferrimagnet, *Nature Comm.* **3**, 666 (2012)
- 654 [8] C. E. Graves et al., Nanoscale Spin Reversal by Nonlocal Angular Momentum Transfer
655 following Ultrafast Laser Excitation in Ferrimagnetic GdFeCo, *Nature Mater.* **12**, 293-298
656 (2013)
- 657 [9] C.-H. Lambert et al., All-Optical Control of Ferromagnetic Thin Films and
658 Nanostructures, *Science* **345**, 1337-1340 (2014)
- 659 [10] S. Mangin et al., Engineered Materials for All-Optical Helicity-Dependent Magnetic
660 Switching, *Nature Mater.* **13**, 286-292 (2014)
- 661 [11] M. S. El Hadri, P. Pirro, C.-H. Lambert, S. Petit-Watelot, Y. Quessab, M. Hehn, F.
662 Motaigue, G. Malinowski, and S. Mangin, Two-Types of All-Optical Magnetisation
663 Switching Mechanisms using Femtosecond Laser Pulses, *Phys. Rev. B* **94**, 064412 (2016)
- 664 [12] M. S. El Hadri, M. Hehn, P. Pirro, C.-H. Lambert, G. Malinowski, E. E. Fullerton and S.
665 Mangin, Domain Size Criterion for the Observation of All-Optical Helicity-Dependent
666 Switching in Magnetic Thin Films, *Phys. Rev. B* **94**, 064419 (2016)
- 667 [13] T.-M. Liu et al., Nanoscale Confinement of All-Optical Magnetic Switching in TbFeCo
668 – Competitions with Nanoscale Heterogeneity, *Nano Letters* **15**, 6862-6868 (2015)
- 669 [14] N. Bergeard, M. Hehn, S. Mangin, G. Lengaigne, F. Motaigue, M. L. M. Laliu, B.
670 Koopmans and G. Malinowski, Hot-Electron-Induced Ultrafast Demagnetisation in Co/Pt
671 Multilayers, *Phys. Rev. Lett.* **117**, 147203 (2016)
- 672 [15] R. B. Wilson, J. Gorchon, Y. Yand, C.-H. Lambert, S. Salahuddin, and J. Bokor,
673 Ultrafast Magnetic Switching of GdFeCo with Electronic Heat Currents, *Phys. Rev. B* **95**,
674 180409 (2017)

- 675 [16] S. Mangin, Ultrafast magnetisation dynamics (towards ultrafast spintronics) in The 2017
676 magnetism roadmap, *J. Phys. D: Appl. Phys.* **50**, 363001 (2017)
- 677 [17] M. Battiato, K. Carva, and P. M. Oppeneer, Superdiffusive Spin transport as a
678 Mechanism of Ultrafast Demagnetisation, *Phys. Rev. Lett.* **105**, 027203 (2010)
- 679 [18] B. Koopmans, G. Malinowski, F. Dalla Longa, D. Steiauf, M. Fähnle, T. Roth, M.
680 Cinchetti, and M. Aeschlimann, Explaining the Paradoxical Diversity of Ultrafast Laser-
681 Induced Demagnetisation, *Nature Mater.* **9**, 259-265 (2009)
- 682 [19] E. Turgut et al., Stoner versus Heisenberg: Ultrafast Exchange Reduction and Magnon
683 Generation during Laser-Induced Demagnetization, *Phys. Rev. B* **94**, 220408(R) (2016)
- 684 [20] M. Djordjevic and M. Münzenberg, Connecting the Timescales in Picosecond
685 Remagnetisation Experiments, *Phys. Rev. B* **75**, 012404 (2007)
- 686 [21] B. Rumpf and A. C. Newell, Coherent Structures and Entropy in Constrained,
687 Modulationally Unstable, Nonintegrable Systems, *Phys. Rev. Lett.* **87**, 054102 (2001)
- 688 [22] A. Kosevich, B. Ivanov, and A. Kovalev, Magnetic Solitons, *Phys. Rep.* **194**, 117-238
689 (1990)
- 690 [23] E. Iacocca, T. J. Silva, and M. A. Hofer, Breaking of Galilean Invariance in the
691 Hydrodynamic Formulation of Ferromagnetic Thin Films, *Phys. Rev. Lett.* **118**, 017203
692 (2017)
- 693 [24] E. Iacocca, T. J. Silva, and M. A. Hofer, Symmetry-Broken Dissipative Exchange
694 Flows in Thin-Film Ferromagnets with In-Plane Anisotropy, *Phys. Rev. B* **96**, 134434 (2017)
- 695 [25] M. Maiden, L. D. Bookman, and M. A. Hofer, Attraction, Merger, Reflection, and
696 Annihilation in Magnetic Droplet Soliton Scattering, *Phys. Rev. B* **89**, 180409(R) (2014)
- 697 [26] G. Mazenko, Chapter 11. Unstable growth, in *Nonequilibrium Statistical Mechanics*,
698 Weinheim, Wiley-VCH, 2006, pp. 403 - 453.
- 699 [27] A. J. Bray, Theory of Phase-Ordering Kinetics, *Adv. Phys.* **43**, 357-459 (1994)
- 700 [28] S. T. Bramwell, M. F. Faulkner, P. C. W. Holdsworth, and A. Taroni, Phase Order in
701 Superfluid Helium Films, *Europhys. Lett.* **112**, 56003 (2015)
- 702 [29] D. Laroze, P. Díaz, and R. L. Stamps, Scaling Laws of Dipolar Magnetic Systems at
703 Finite Temperature, *Phys. Rev. B* **95**, 104438 (2017)
- 704 [30] K. Shimizu, Y. Kuno, T. Hirano, and I. Ichinose, Dynamics of a Quantum Phase
705 Transition in the Bose-Hubbard Model: Kibble-Zurek Mechanism and Beyond, *Phys. Rev. A*
706 **97**, 033626 (2018)
- 707 [31] C. Rotschild, T. Schwartz, O. Cohen, and M. Segev, Incoherent Spatial Solitons in
708 Effectively Instantaneous Nonlinear Media, *Nature Photonics* **2**, 371-376 (2008)
- 709 [32] T. W. B. Kibble, Topology of Cosmic Domains and Strings, *J. Phys. A* **9**, 1387 (1976)
- 710 [33] W. H. Zurek, Cosmological Experiments in Superfluid Helium?, *Nature* **317**, 505-508
711 (1985)

- 712 [34] S. Eckel, A. Kumar, T. Jacobson, I. B. Spielman, and G. K. Campbell, A Rapidly
713 Expanding Bose-Einstein Condensate: an Expanding Universe in the Lab, *Phys. Rev. X* **8**,
714 021021 (2018)
- 715 [35] S.-Z. Lin et al., Topological Defects as Relics of Emergent Continuous Symmetry and
716 Higgs Condensation of Disorder in Ferroelectrics, *Nature Phys.* **10**, 970-977 (2014)
- 717 [36] T. Eggebrecht, M. Möller, J. G. Gatzmann, N. Rubiano da Silva, A. Feist, U. Martens,
718 H. Ulrichs, M. Münzenberg, C. Ropers, and S. Schäfer, Light-Induced Metastable Magnetic
719 Texture Uncovered by In-Situ Lorentz Microscopy, *Phys. Rev. Lett.* **118**, 097203 (2017)
- 720 [37] S.-G. Je et al., Creation of Magnetic Skyrmion Bubble Lattices by Ultrafast Laser in
721 Ultrathin Films, *Nano Lett.* **18**, 7362-7371 (2018)
- 722 [38] H. Dürr, J. F. Wendelken, and J.-K. Zuo, Island Morphology and Adatom Energy
723 Barriers During Homoepitaxy on Cu(001), *Surf. Sci.* **328**, L527 (1995)
- 724 [39] P. W. Granitzka et al., Magnetic Switching in Granular FePt Layers Promoted by Near-
725 Field Laser Enhancement, *Nano Letters* **17**, 2426-2432 (2017)
- 726 [40] T. A. Ostler et al., Crystallographically Amorphous Ferrimagnetic Alloys: Comparing a
727 Localized Atomistic Spin Model with Experiments, *Phys. Rev. B* **84**, 024407 (2011)
- 728 [41] R. F. L. Evans, W. J. Fan, P. Churemart, T. A. Ostler, M. A. A. Allis, and R. W.
729 Chantrell, Atomistic Spin Model Simulations of Magnetic Nanomaterials, *J. Phys: Condens.*
730 *Matter.* **26**, 103202 (2014)
- 731 [42] A. Hubert and R. Schafer, *Magnetic Domains*, Berlin Heidelberg New York, Springer
732 (2009)
- 733 [43] L. D. Landau and E. Lifshitz, On the Theory of the Dispersion of Magnetic Permeability
734 in Ferromagnetic Bodies, *Phys. Z. Sowjet* **8**, 153 (1953)
- 735 [44] D. Kip, M. Soljacic, M. Segev, E. Eugenieva, D. N. Christodoulides, Modulation
736 instability and pattern formation in spatially incoherent light beams, *Science* **290**, 495-498
737 (2000)
- 738 [45] M. Soljacic, M. Segev, T. Coskun, D. N. Christodoulides, and A. Vishwanath,
739 Modulation Instability of Incoherent Beams in Noninstantaneous Nonlinear Media, *Phys.*
740 *Rev. Lett.* **84**, 467 (2000)
- 741 [46] K. E. Strecker, G. B. Partridge, A. G. Truscott, and R. G. Hulet, Formation and
742 propagation of matter-wave soliton trains, *Nature* **417**, 150-153 (2002)
- 743 [47] K.-I. Murata and H. Tanaka, Microscopic Identification of the Order Parameter
744 Governing Liquid-Liquid Transition in a Molecular Liquid, *P. Natl. Acad. Sci. USA* **112**,
745 5956-5961 (2105)
- 746 [48] I. M. Lifshitz, Kinetics of Ordering During Second-Order Phase Transitions, *Sov. Phys.*
747 *JETP* **15**, 939 (1962)
- 748 [49] E. Allen and J. W. Cahn, A Microscopic Theory for Antiphase Boundary Motion and its
749 Application to Antiphase Domain Coarsening, *Acta Metall.* **27**, 1085-1095 (1979)

750 [50] H. C. Fogedby and O. G. Mouritsen, Lifshitz-Allen-Cahn Domain-Growth Kinetics of
751 Ising Models with Conserved Density, *Phys. Rev. B* **37**, 5962 (1988)

752 [51] M. P. Anderson, D. J. Srolovitz, G. S. Grest, and P. S. Sahni, Computer Simulation of
753 Grain Growth I. Kinetics, *Acta Metall.* **32**, 783-791 (1984)

754 [52] B. I. Halperin and P. C. Hohenberg, Hydrodynamic Theory of Spin Waves, *Phys. Rev.*
755 **188**, 989 (1969)

756 [53] J. König, M. C. Bønsager, and A. M. MacDonald, Dissipationless Spin Transport in
757 Thin Film Ferromagnets, *Phys. Rev. Lett.* **87**, 187202 (2001)

758 [54] P. Bruno and V. K. Dugaev, Equilibrium Spin Currents and the Magnetoelectric Effect
759 in Magnetic Nanostructures, *Phys. Rev. B* **72**, 241308 (2005)

760 [55] D. C. Ralph and M. D. Stiles, Spin Transfer Torques, *J. Magn. Magn. Mater* **320**, 1190-
761 1216 (2008)

762 [56] D. Xiao, V. Tiberkevich, Y. H. Liu, Y. W. Liu, S. M. Mohseni, S. Chung, M. Ahlberg,
763 A. N. Slavin, J. Åkerman, and Y. Zhou, Parametric Autoexcitation of Magnetic Droplet
764 Soliton Perimeter Modes, *Phys. Rev. B* **95**, 024106 (2017)

765 [57] H.-B. Braun, Topological Effects in Nanomagnetism: from Superparamagnetism to
766 Chiral Quantum Solitons, *Adv. Phys.* **61**, 1-116 (2012)

767 [58] W. F. Schlotter et al., The Soft X-Ray Instrument for Materials Studies and the Linac
768 Coherent Light Source X-Ray Free-Electron Laser, *Rev. Sci. Instrum.* **83**, 043107 (2012)

769 [59] M. Beye et al., X-Ray Pulse Preserving Single-Shot Optical Cross-Correlation Method
770 for Improved Experimental Temporal Resolution, *Appl. Phys. Lett.* **100**, 121108 (2012)

771 [60] S. I. Anisimov, B. L. Kapeliovich, and T. L. Perelman, Electron Emission From Metal
772 Surfaces Exposed to Ultrashort Laser Pulses, *Sov. Phys. JETP* **39**, 375 (1974)

773 [61] A. Vansteenkiste, J. Leliaert, M. Dvornik, M. Helsen, F. Garcia-Sanchez and B. Van
774 Waeyenberge, The Design and Verification of Mumax3, *AIP Advances* **4**, 107133 (2014)

775

776

777 **End Notes**

778 **Acknowledgements**

779 This material is based upon work supported by the U.S. Department of Energy, Office of
780 Science, Office of Basic Energy Sciences under Award Number 0000231415 and DE-
781 SC0017643, and is partly supported by the European Research Council ERC Grant
782 agreement No. 339813 (Exchange) and the Netherlands Organisation for Scientific Research
783 (NWO). Operation of LCLS is supported by the U.S. Department of Energy, Office of Basic
784 Energy Sciences under contract No. DE-AC02-76SF00515. This work used the ARCHER
785 UK National Supercomputing Service (<http://www.archer.ac.uk>). This project has received
786 funding from the European Union's Horizon 2020 research and innovation programme under
787 grant agreement No. 737093 (FEMTOTERABYTE). This work was performed using
788 resources provided by the Cambridge Service for Data Driven Discovery (CSD3) operated by
789 the University of Cambridge Research Computing Service (<http://www.csd3.cam.ac.uk/>),
790 provided by Dell EMC and Intel using Tier-2 funding from the Engineering and Physical
791 Sciences Research Council (capital grant EP/P020259/1), and DiRAC funding from the
792 Science and Technology Facilities Council (www.dirac.ac.uk). E.I. acknowledges support
793 from the Swedish Research Council, Reg. No. 637-2014-6863. M.A.H. was partially
794 supported by NSF CAREER DMS-1255422. L.L.G. would like to thank the
795 VolkswagenStiftung for the financial support through the Peter-Paul-Ewald Fellowship.
796 R.W.C. is grateful to Radboud University, Nijmegen, for hospitality under the Radboud
797 excellence scheme. E.I. thanks Leo Radzihovsky for fruitful discussions.

798

799 **Author contributions**

800 E.I. performed micromagnetic simulations. A.T. prepared the samples. A.H.R., T.-M.L.,
801 P.W.G., E.J., A.X.G., S.B., C.E.G., R.K., Z.C., D.J.H., T.C., L.L.G., K.H., H.O., W.F.S.,
802 G.L.D., G.C., M.C.H., S.C., A.K., A.V.K., T.R., J.S., and H.A.D. performed experiments.
803 Z.F. and R.F.L.E. performed atomistic simulations. R.F.L.E. developed the numerical
804 representation of Fe and Gd inhomogeneities in the atomistic model. Z.F., S.R., R.F.L.E.,
805 T.O. and R.W.C. analysed the atomistic data. T.-M.L. and D.H. analysed the experimental
806 data. E.I., M.A.H., and T.J.S. fitted the data and analysed the micromagnetic simulations. All
807 authors contributed to discussions, data analysis, and writing the manuscript.

808

809 **Competing interests**

810 One of the authors, K.H., is an editor on the staff of Nature Communications, but was not in
811 any way involved in the journal review process.

812

813 **Figure 1. Schematic of the experimental setup.** A femtosecond optical pulse randomises
814 the spin degree of freedom and a subsequent circularly polarised X-ray pulse probes the
815 perpendicular magnetisation, m_z , at a given delay, Δt . For each time delay, the two-
816 dimensional X-ray scattering intensity map is obtained, from which the spin-spin correlation
817 function can be extracted. X-ray magnetic circular dichroism is simultaneously measured by
818 the un-scattered beam.

819

820 **Figure 2. Schematic examples of scattered intensities from real-space features.** The left
821 column shows real-space patterns while the right column shows the corresponding scattered
822 intensity computed via Fourier transform with colour scale in arbitrary units. In the top row, a
823 random distribution of circular, localised textures gives rise to a broad feature centred at $q = 0$
824 in the scattered intensity. In the bottom row, localised textures possessing long-range
825 correlations result in a ring pattern in the scattered intensity.

826

827 **Figure 3. Experimental XMCD and spin-spin correlation.** XMCD data is shown in **a** non-
828 AOS obtained in a 30 nm-thick sample subject to an absorbed fluence of 3.91 mJ cm^{-2} and **b**
829 for AOS obtained in a 20 nm-thick sample subject to an absorbed fluence of 4.39 mJ cm^{-2} .
830 Solid lines are guides to the eye. **c** Contours of the azimuthally averaged spin-spin correlation
831 function, $\Delta S^2(q, t)$, for non-AOS. For the time instances indicated by dotted vertical lines,
832 lineouts are shown by black curves in **d** and are vertically shifted for clarity. Fits to the data
833 with a Lorentzian line-shape for the low- q diffraction ring below $q = 0.01 \text{ nm}^{-1}$ and a
834 Gaussian line-shape for the high- q diffraction ring above $q = 0.4 \text{ nm}^{-1}$ are shown by dashed
835 red curves. The black circles indicate the fitted ring radius of the Gaussian component. **e**
836 Contours of the azimuthally averaged spin-spin correlation function, $\Delta S^2(q, t)$, for AOS. For
837 the time instances indicated by dotted vertical lines, lineouts are shown by black curves in **f**
838 and are also vertically shifted for clarity. Fits to the data with a Lorentzian line-shape are
839 shown by dashed red curves.

840

841 **Figure 4. Simulated magnetisation dynamics.** Normalized Gd and Fe average moments
842 from atomistic simulations in the case of **a** non-AOS obtained with a fluence of 10.7 mJ cm^{-2} ,
843 and **b** AOS obtained with a fluence of 11 mJ cm^{-2} . Snapshots of the perpendicular-to-plane
844 magnetisation at 1 ps, 10 ps, and 20 ps for the case of **c** non-AOS and **d** AOS. In both cases,
845 the magnetisation exhibits coarsening of textures.

846

847 **Figure 5. Simulated spin-spin correlation functions.** **a** Contours of the azimuthally
848 averaged spin-spin correlation function obtained from atomistic simulations in the non-AOS
849 case. For the time instances indicated by dotted vertical lines, lineouts are shown by black
850 curves in **b** and are vertically shifted for clarity. Fits using Lorentzian and Gaussian
851 components are shown by red dashed lines. The ring radius of the Gaussian component is
852 shown by black circles. Equivalent plots for the case of AOS are shown in panels **c** and **d**.
853 Fits to the lineouts in this case are obtained by using only a Lorentzian line-shape. For
854 micromagnetic simulations seeded with an atomistic input at 3 ps, the azimuthally averaged
855 spin-spin correlation function and corresponding lineouts and fits are shown in **e** and **f** for
856 non-AOS; and **g** and **h** for AOS.

857 **Figure 6. Imprinted demagnetisation and dissociation for non-AOS.** Fitted parameters of
858 the Gaussian feature from experiments (blue circles) and atomistic simulations (red circles): **a**
859 ring radius, **b** ring width, and **c** normalized amplitude. The appearance of a pattern seeded by
860 the material's chemical inhomogeneity is evidenced by the relatively constant ring radius and
861 ring width within 3 ps after optical pumping accompanied by a growth in the normalized
862 amplitude. At longer times, the magnetic texture dissociates from the chemical
863 inhomogeneities evidenced by the sudden drop of the experimental ring radius and a drop in
864 the atomistic amplitude. Error bars represent standard deviation.

865

866 **Figure 7. Magnon localisation and coalescence.** The ring radius of the Lorentzian feature is
867 shown in **a** for non-AOS and **b** AOS. Time is plotted in logarithmic scale. Symbols represent
868 experimental (blue circles), atomistic (red circles), and micromagnetic (black circles) data.
869 The average magnon drop diameter $L(t)$ is shown in log-log scale for **c** non-AOS and **d** AOS.
870 Dotted lines with corresponding colour code are power-law fits. The magenta solid line
871 indicates the Lifshitz-Cahn-Allen power law. While $L(t)$ increases according to a power law
872 for all cases, the expanding ring radius is a signature of magnon localisation, indicated by the
873 gold-shaded area. The shrinking ring radius observed only for the non-AOS case is the
874 signature of magnon coalescence, indicated by the blue-shaded area. Error bars represent
875 standard deviation.

876

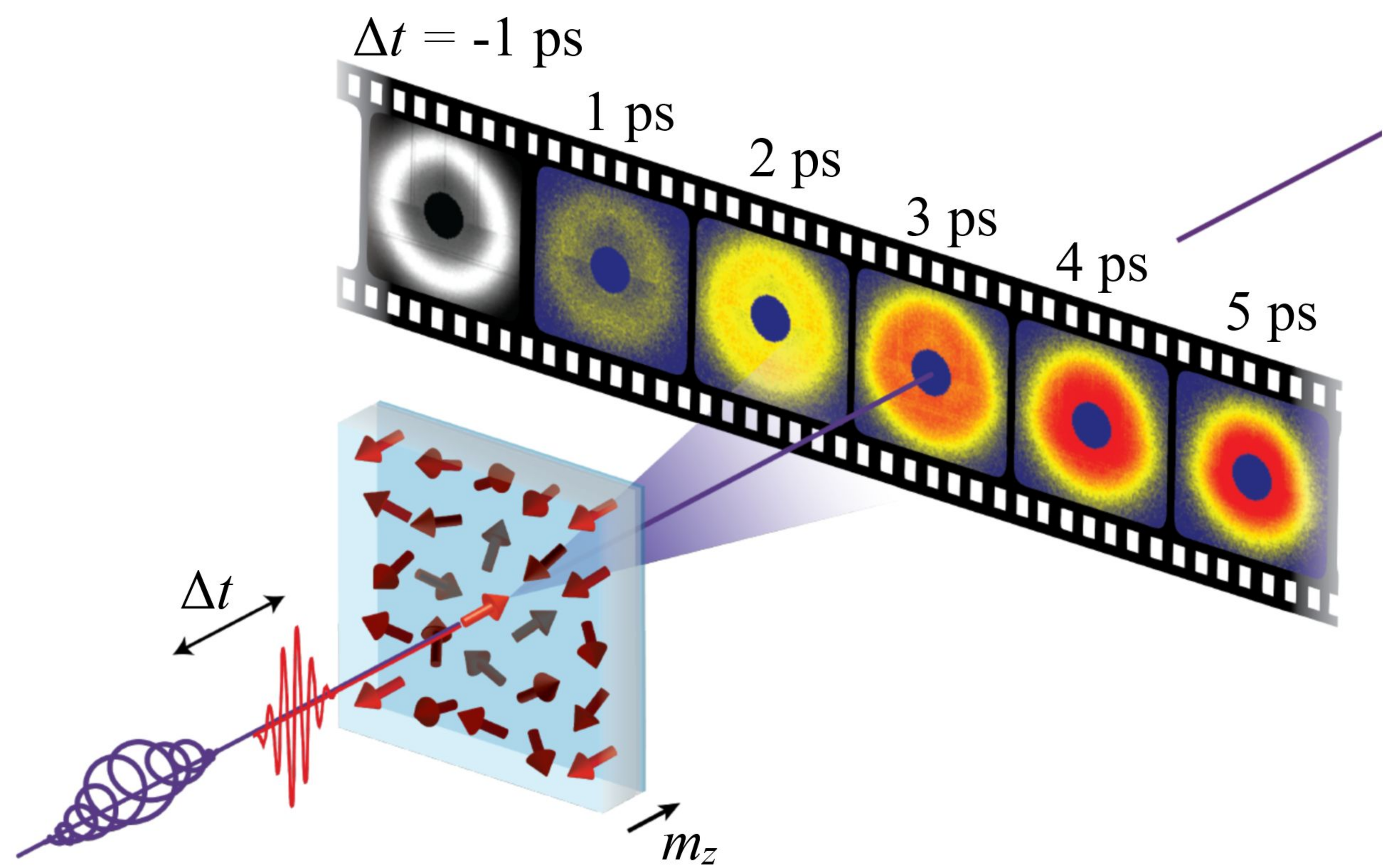
877 **Figure 8. Large transfer of angular momentum.** The snapshots show the evolution of
878 magnon drops, including merger and break-up. The black areas represent magnon drop
879 perimeters ($|m_z| < 0.2$) and the white and grey areas indicate that the perpendicular-to-plane
880 magnetisation is preferentially parallel or antiparallel to the applied field. The pink-shaded
881 curves represent EFSCs expressed as equivalent 100% spin polarised charge current. The
882 streamlines indicate the instantaneous transfer of perpendicular-to-plane angular momentum.

883

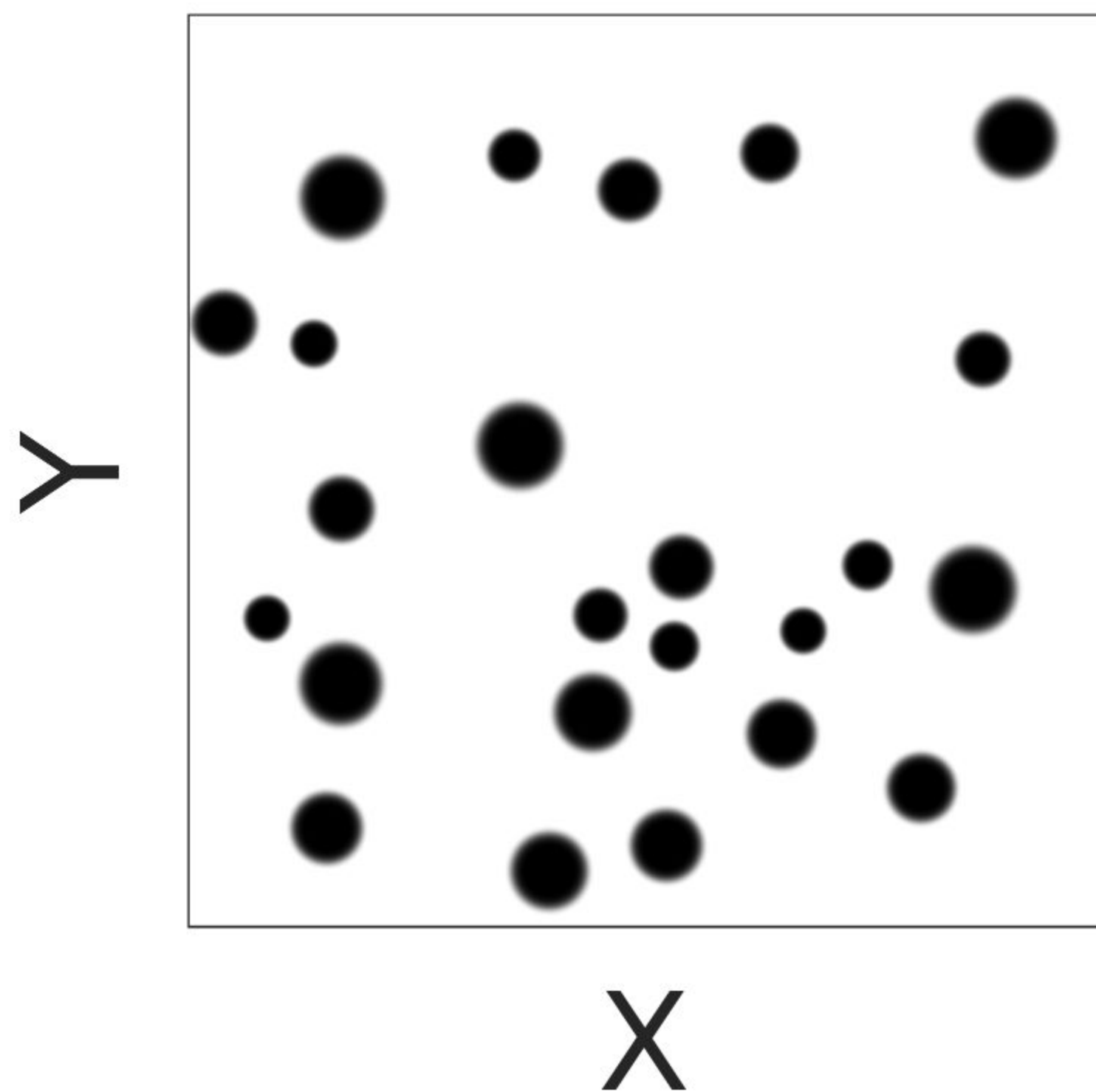
		Experiment	Atomistic simulations	Micromagnetic simulations
Non-AOS	a	0.88 ± 0.01	0.71 ± 0.01	0.89 ± 0.007
	b	4.36 ± 0.11	6.71 ± 0.25	1.95 ± 0.05
AOS	a	1.14 ± 0.15	0.78 ± 0.03	0.77 ± 0.01
	b	10.84 ± 3.97	12.68 ± 0.79	2.99 ± 0.15

884 **Table 1. Fitted parameters for the power law $L(t) = bt^t$**

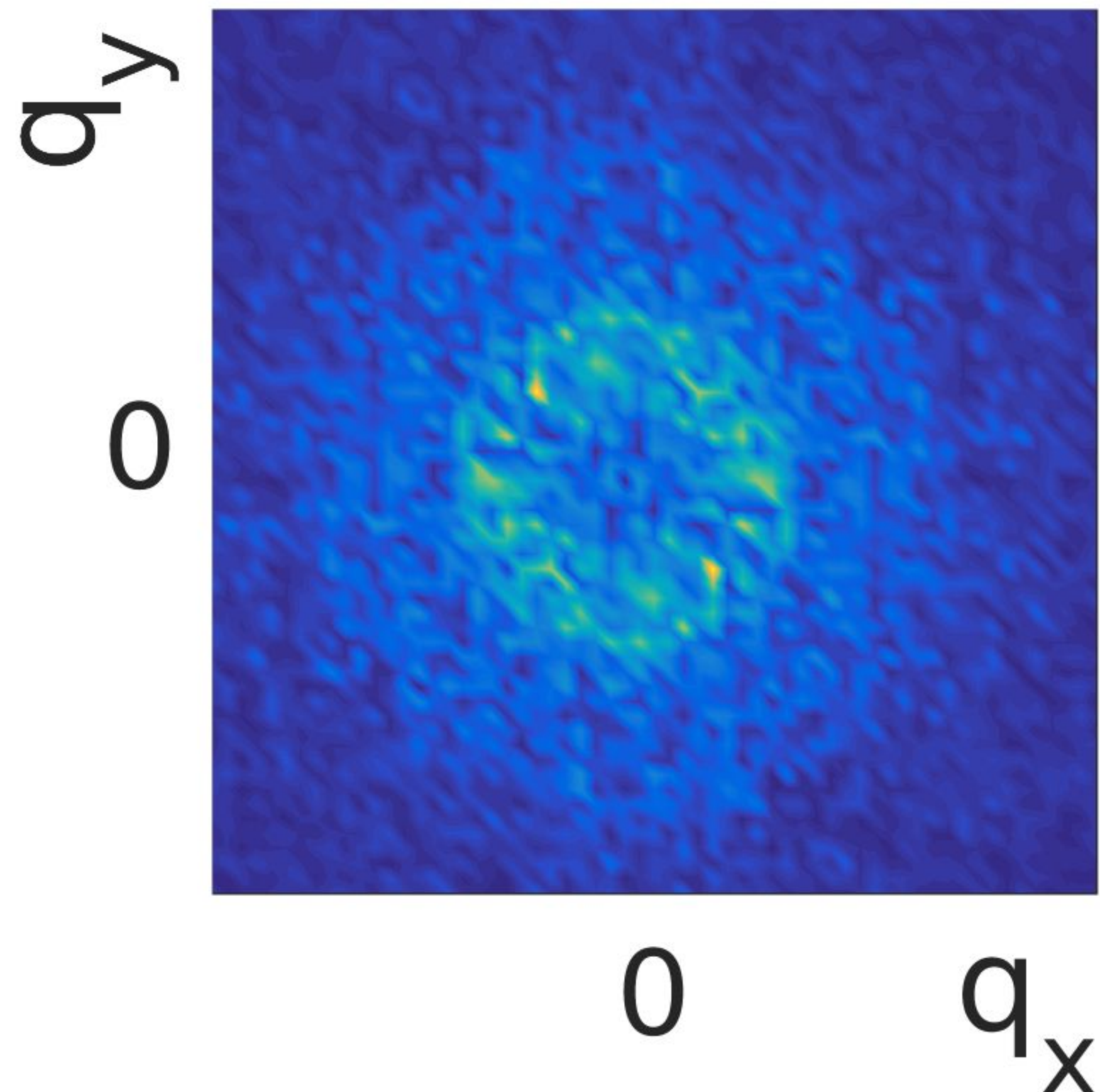
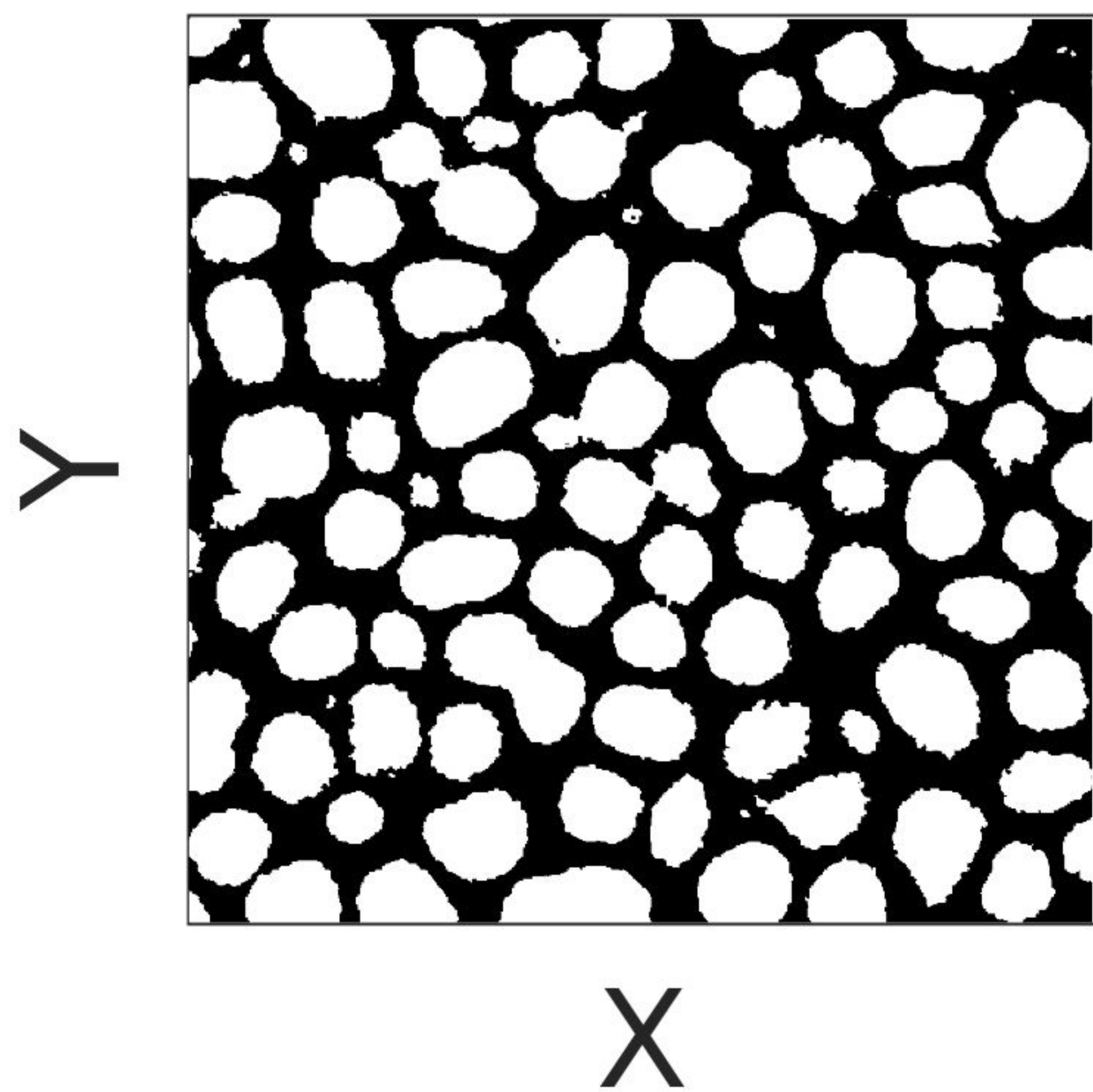
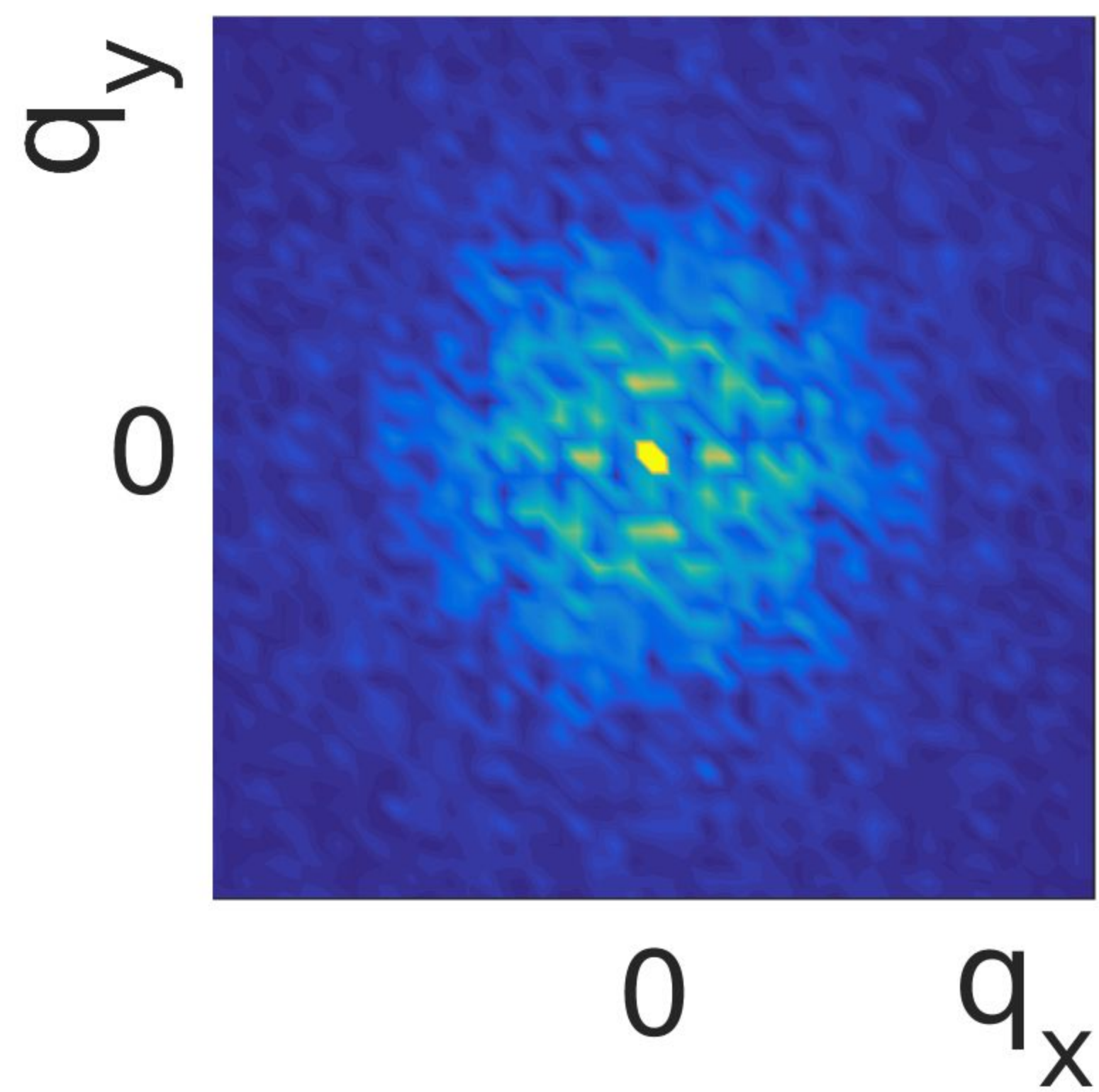
885

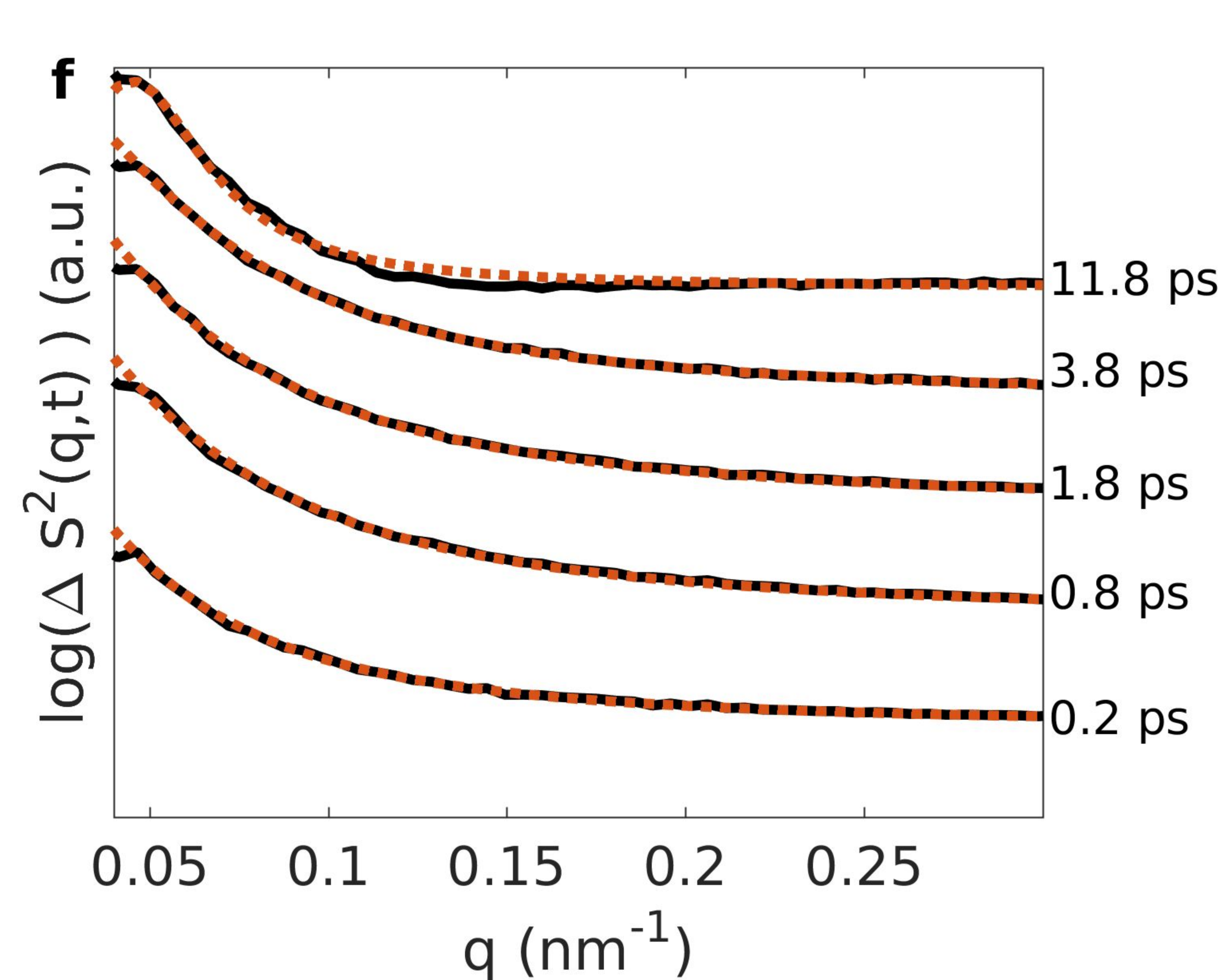
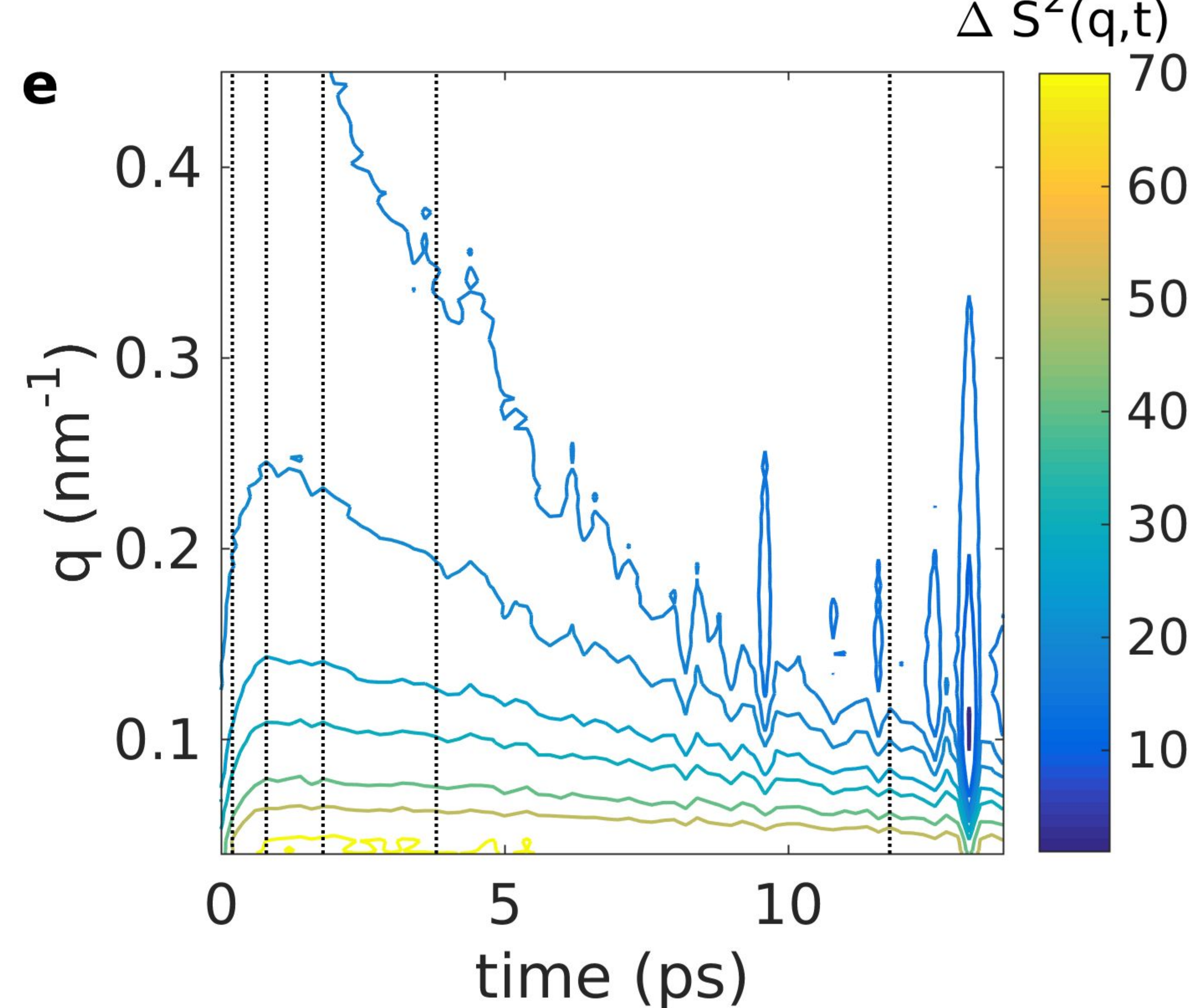
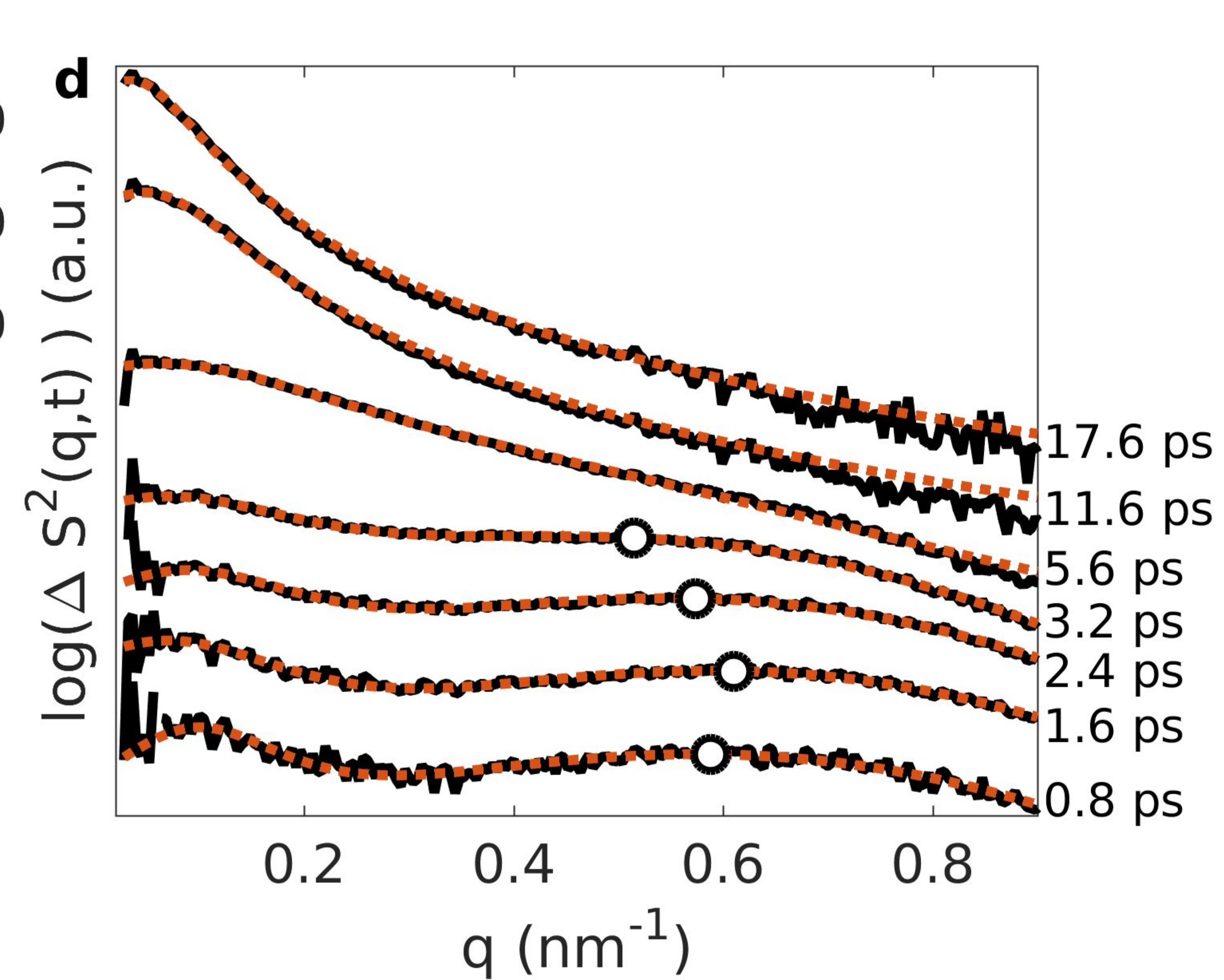
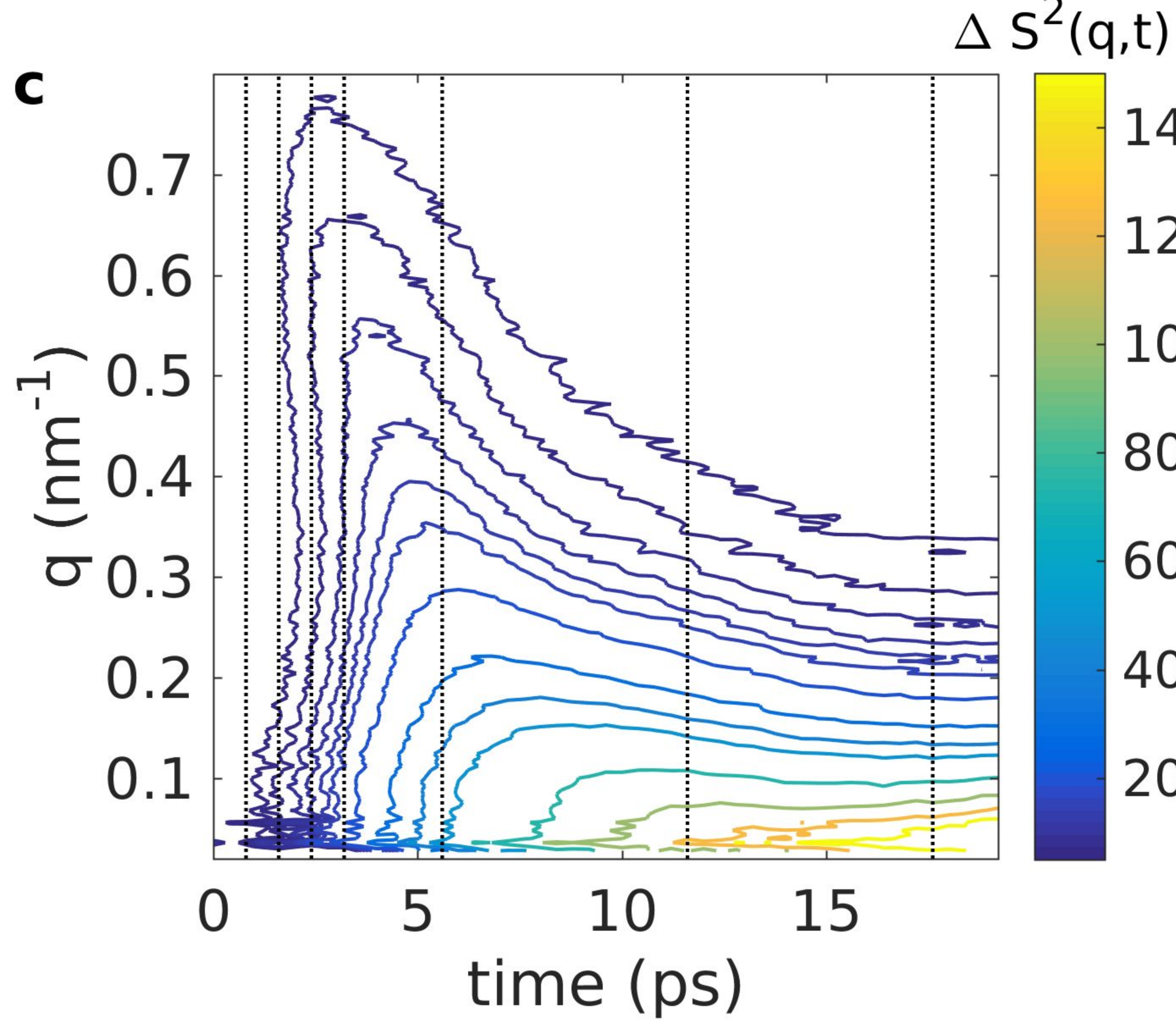
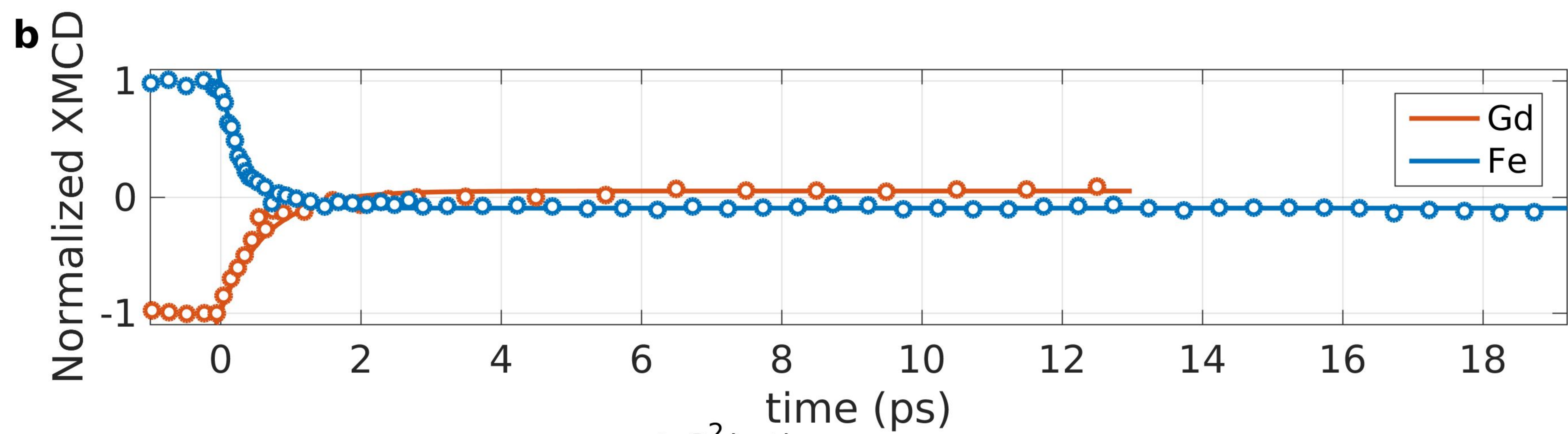
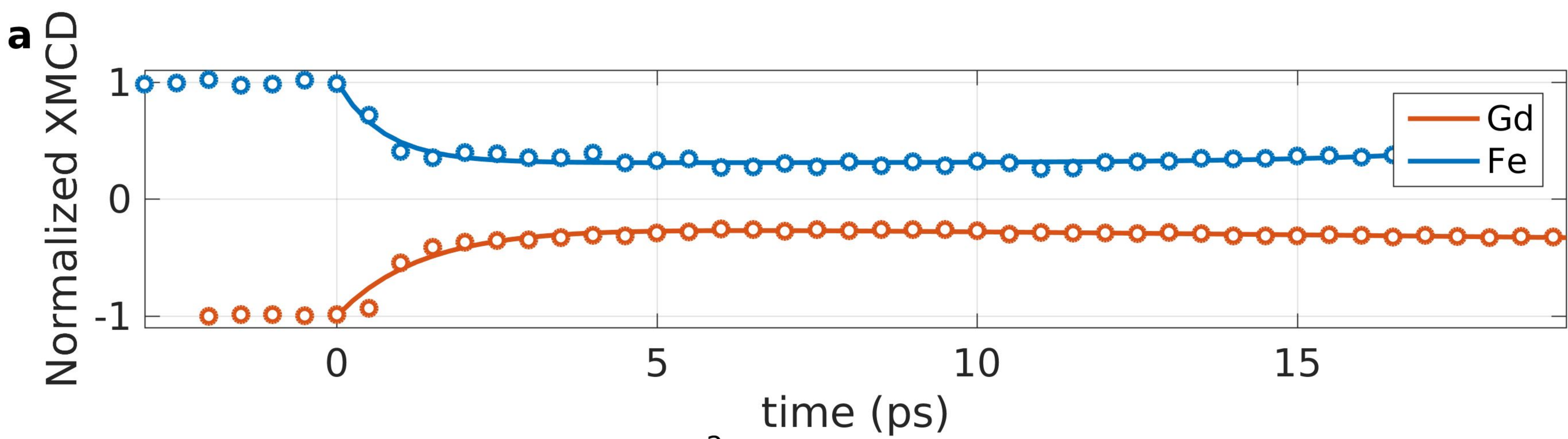


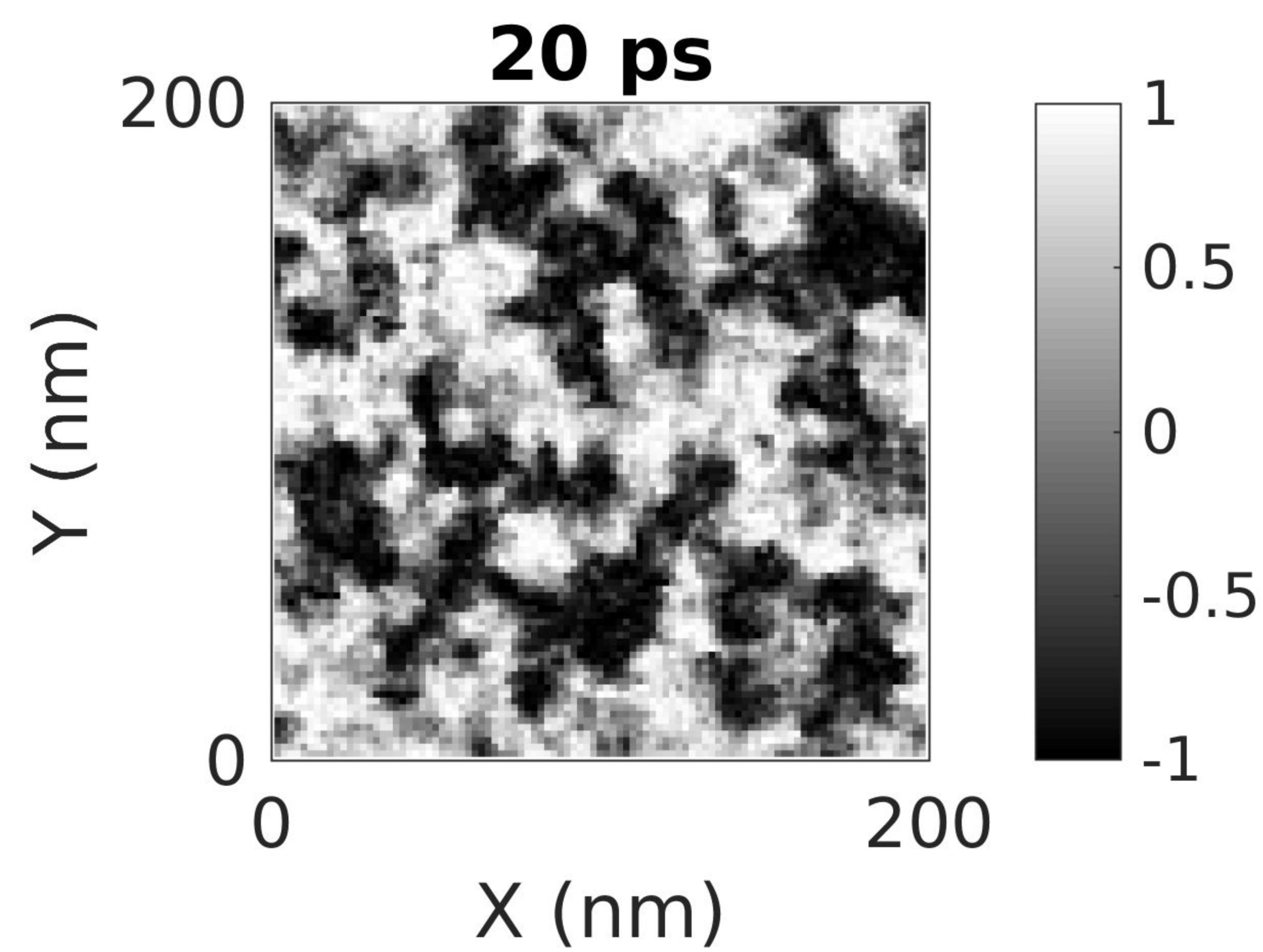
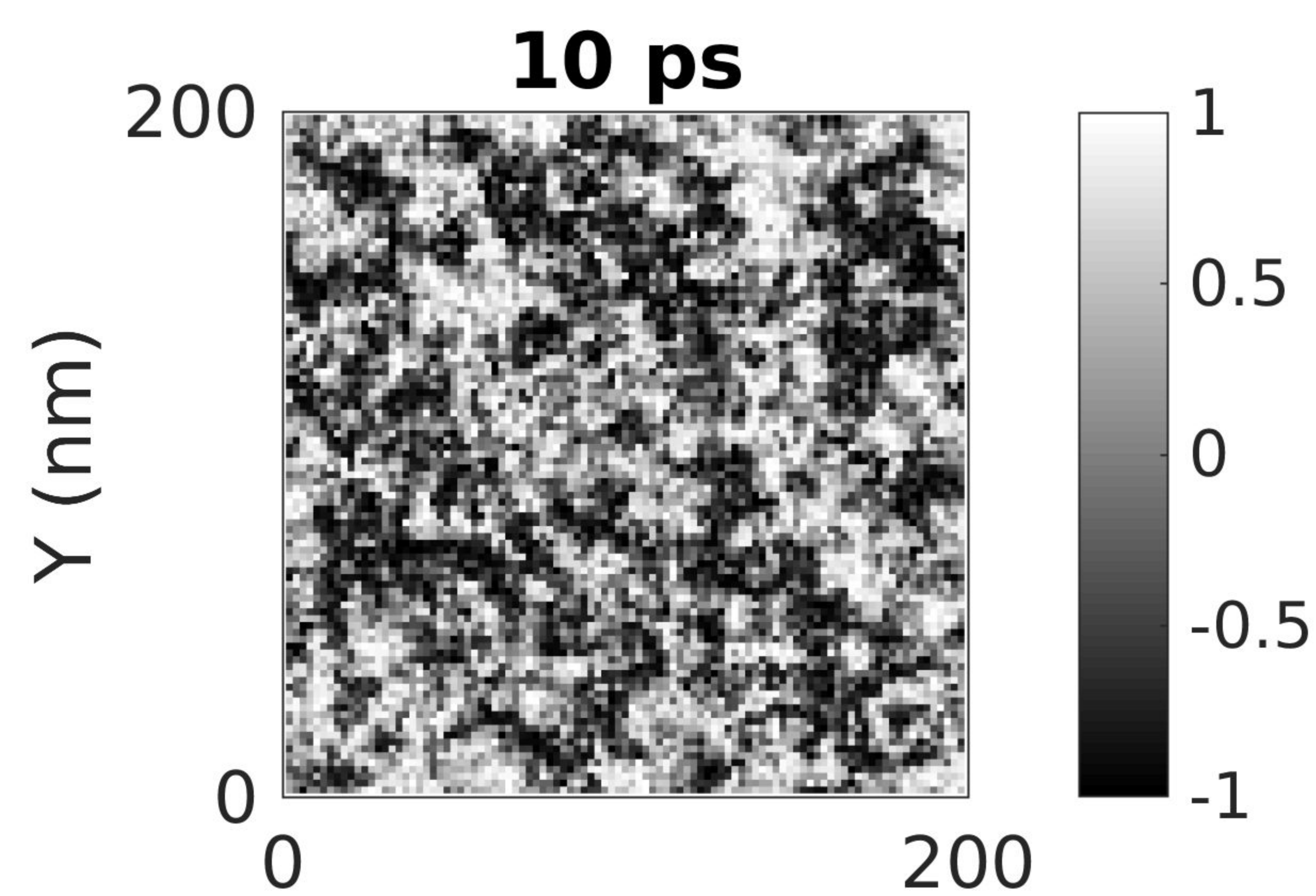
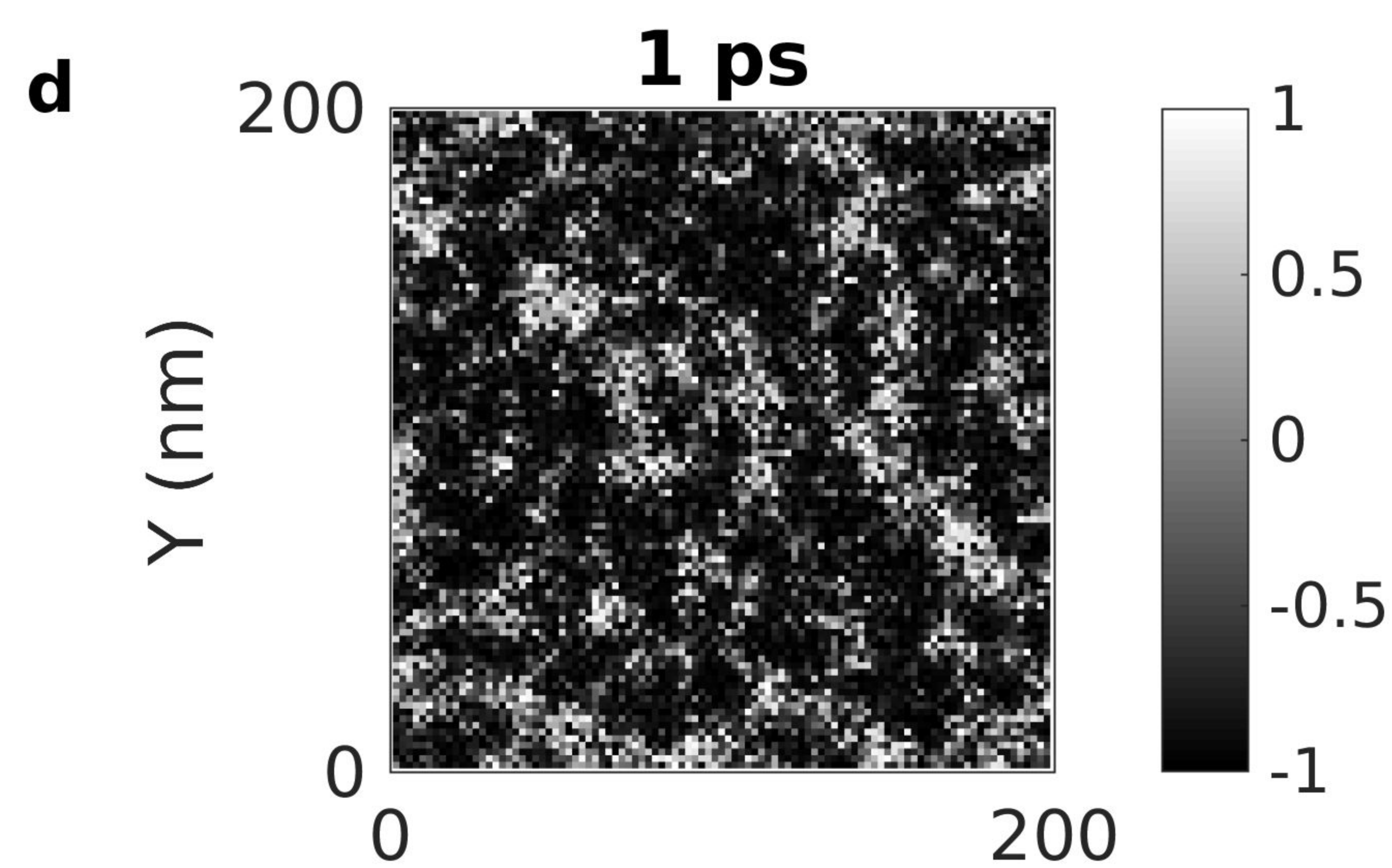
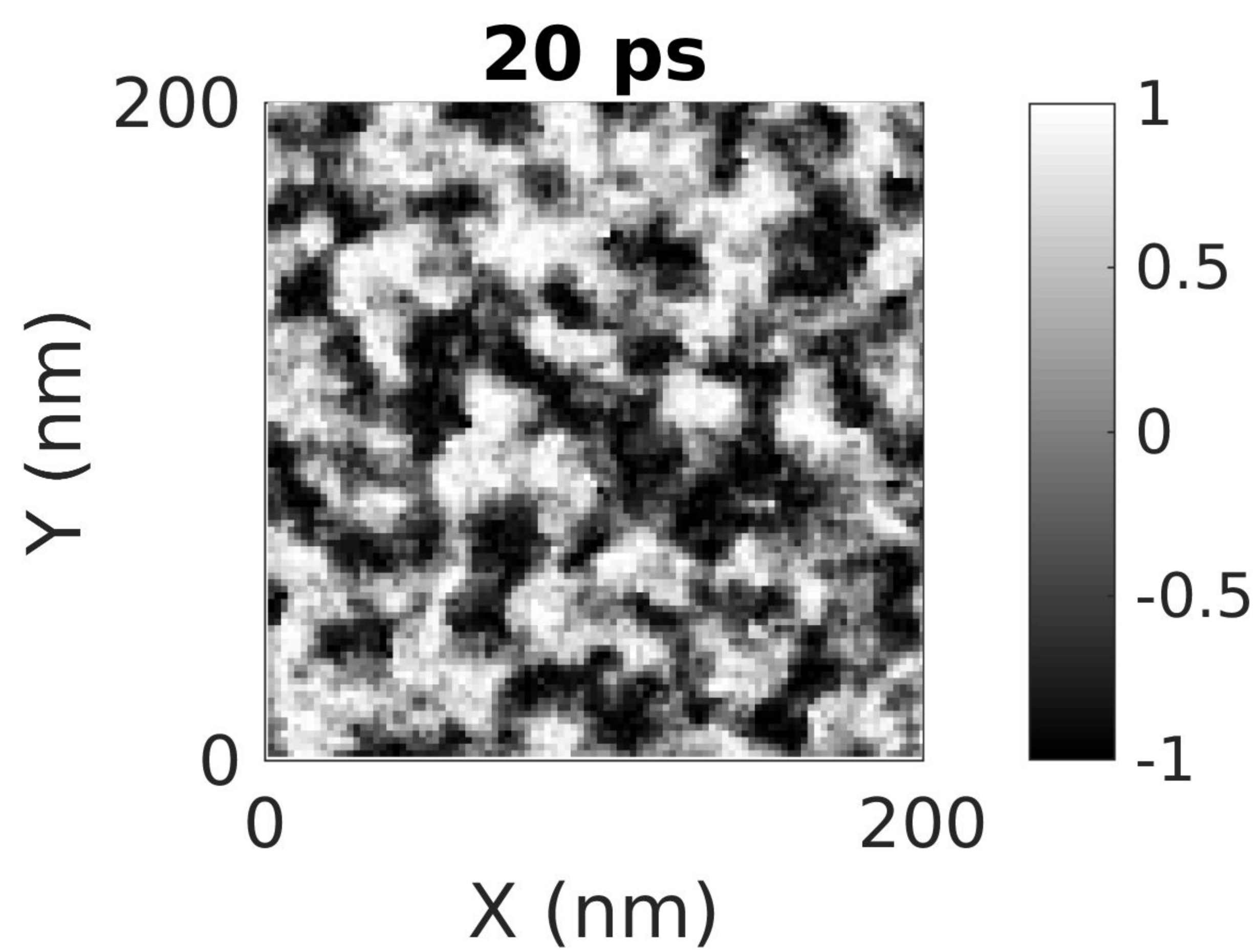
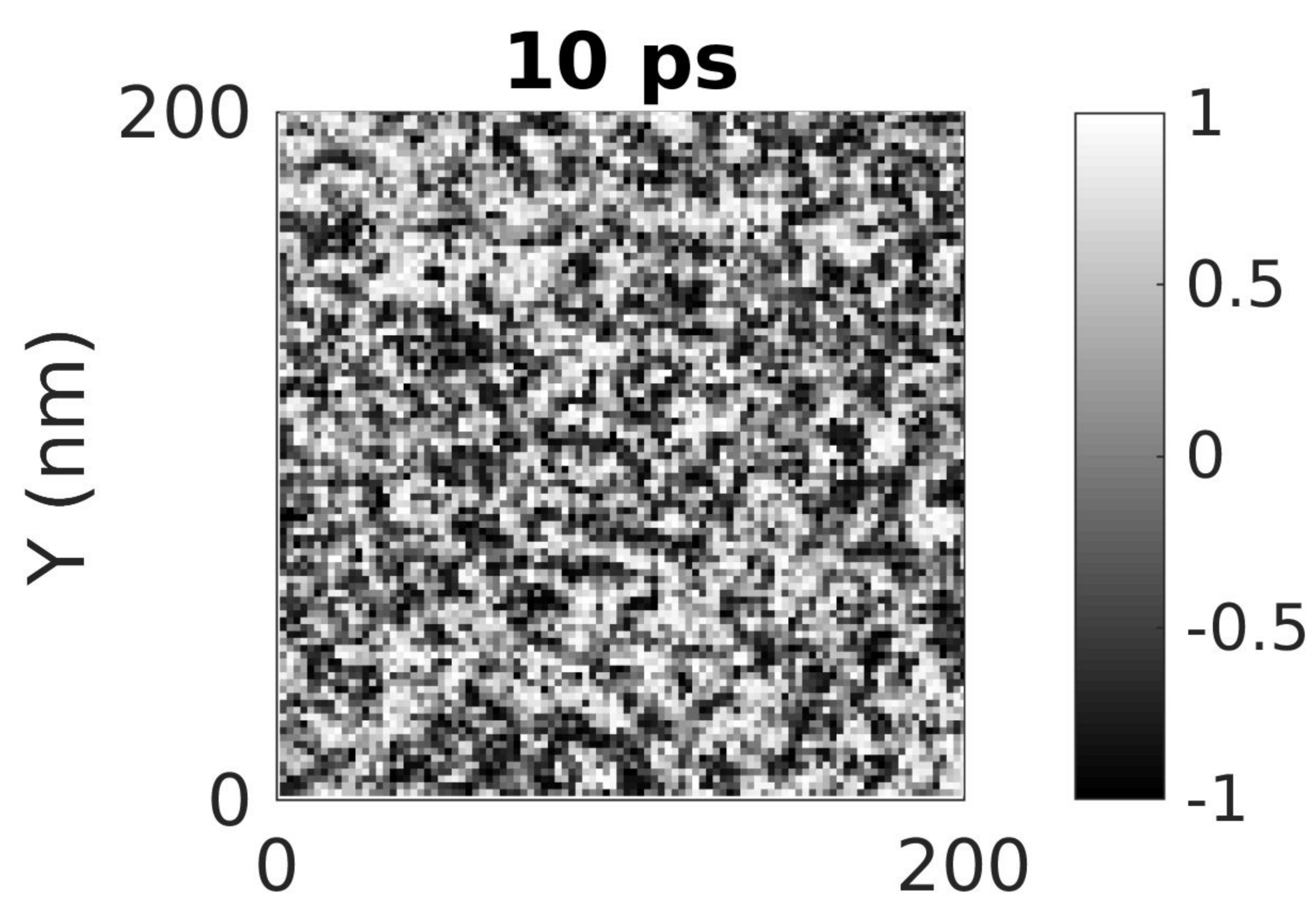
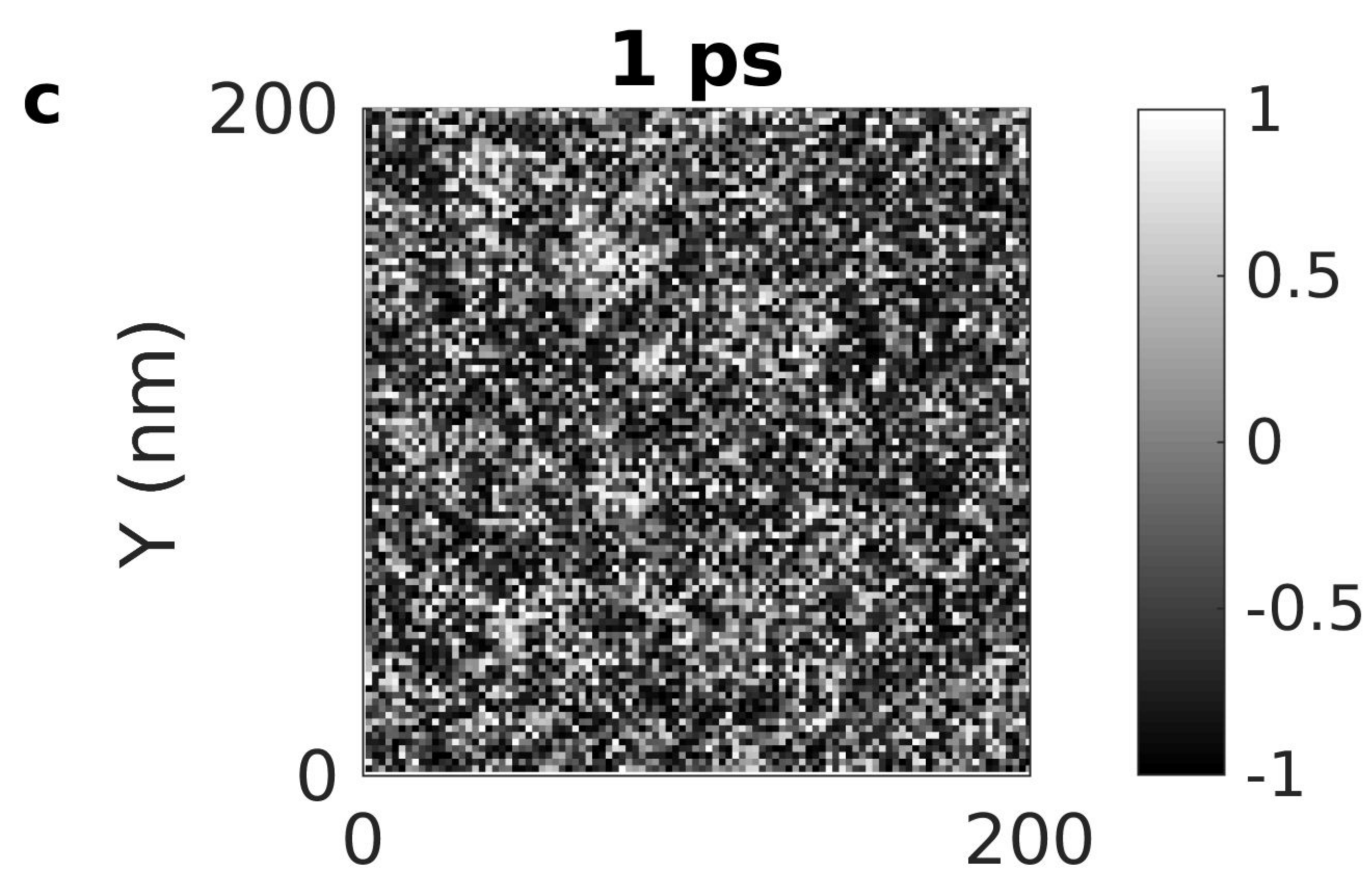
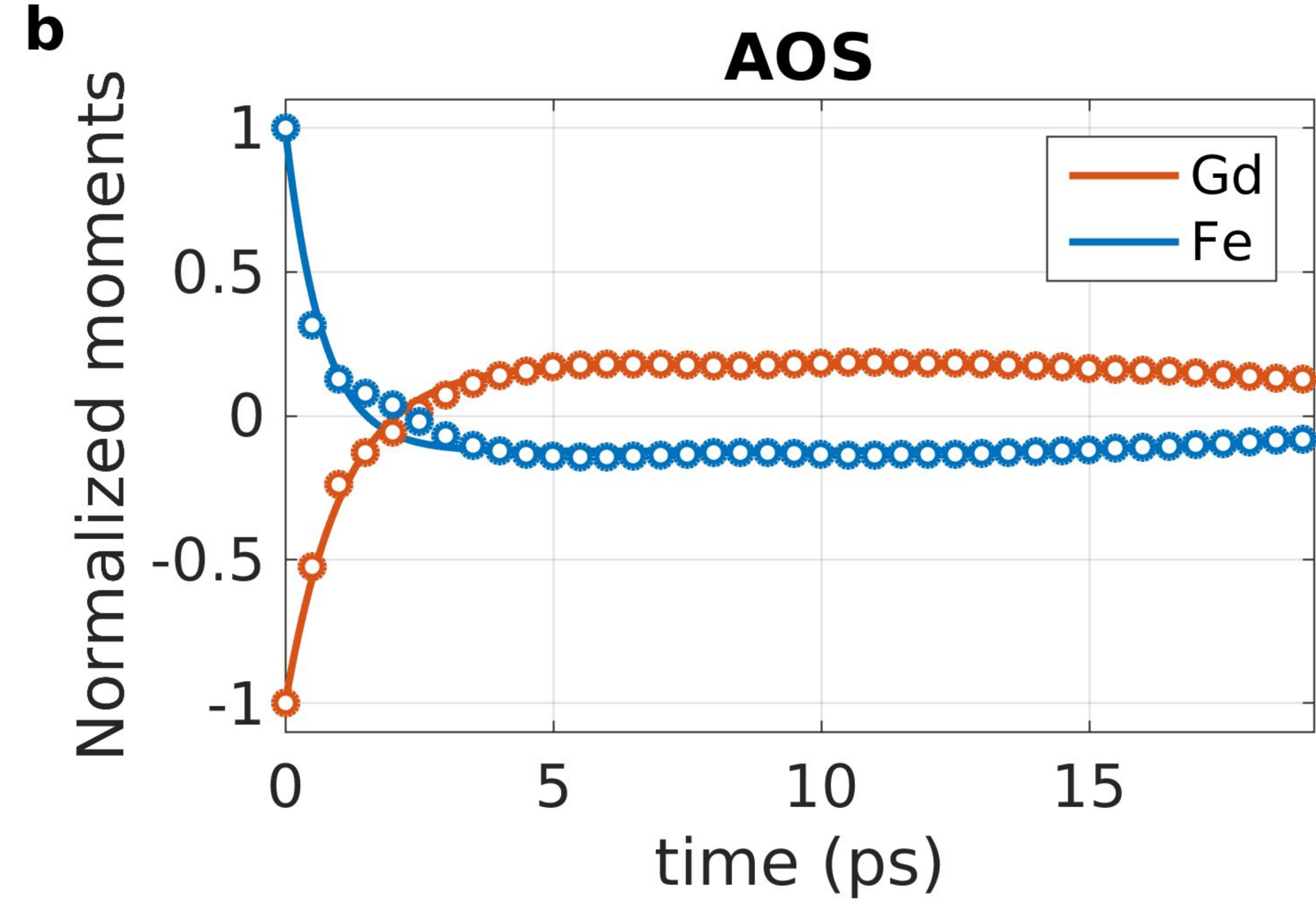
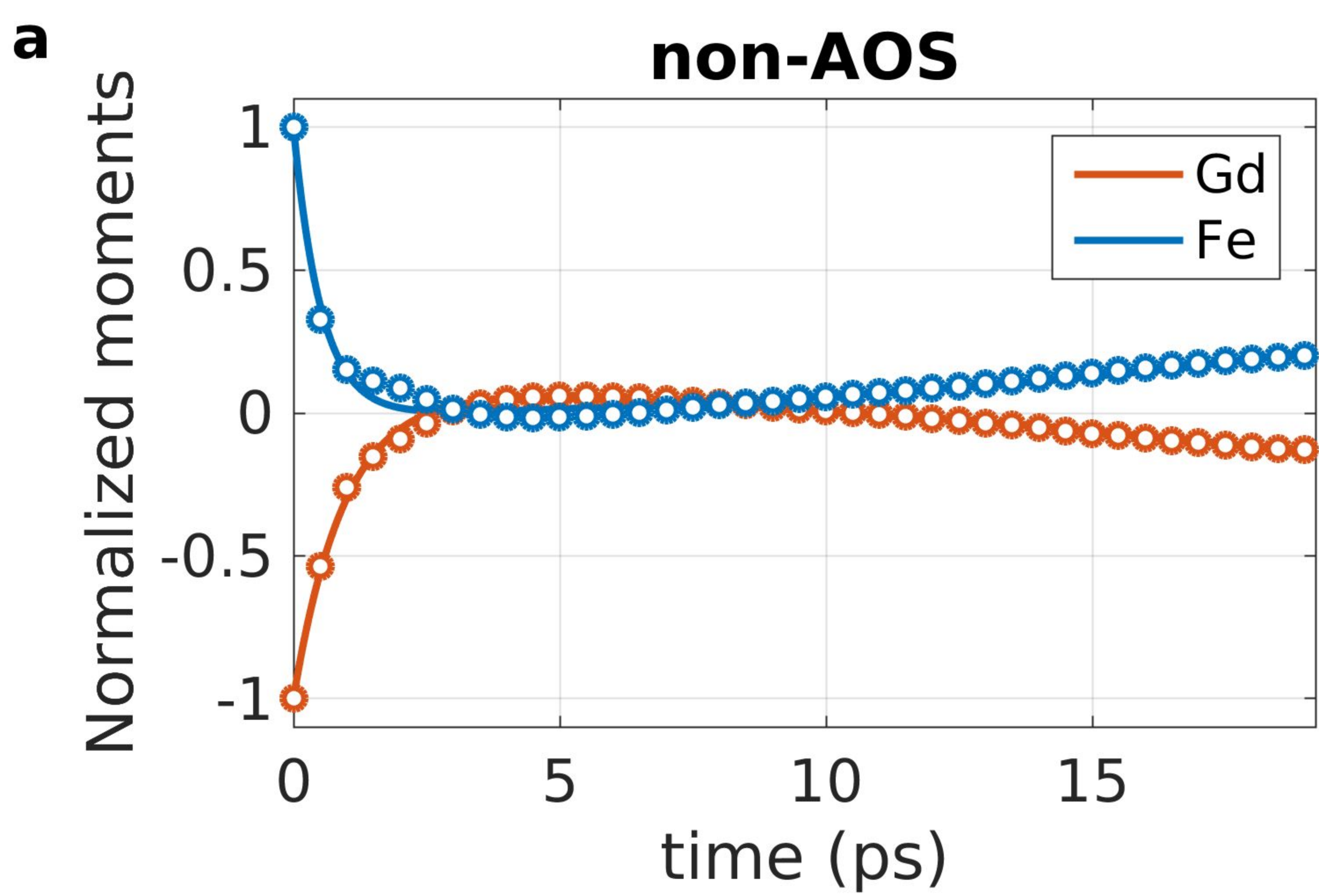
Real space



Scattered intensity



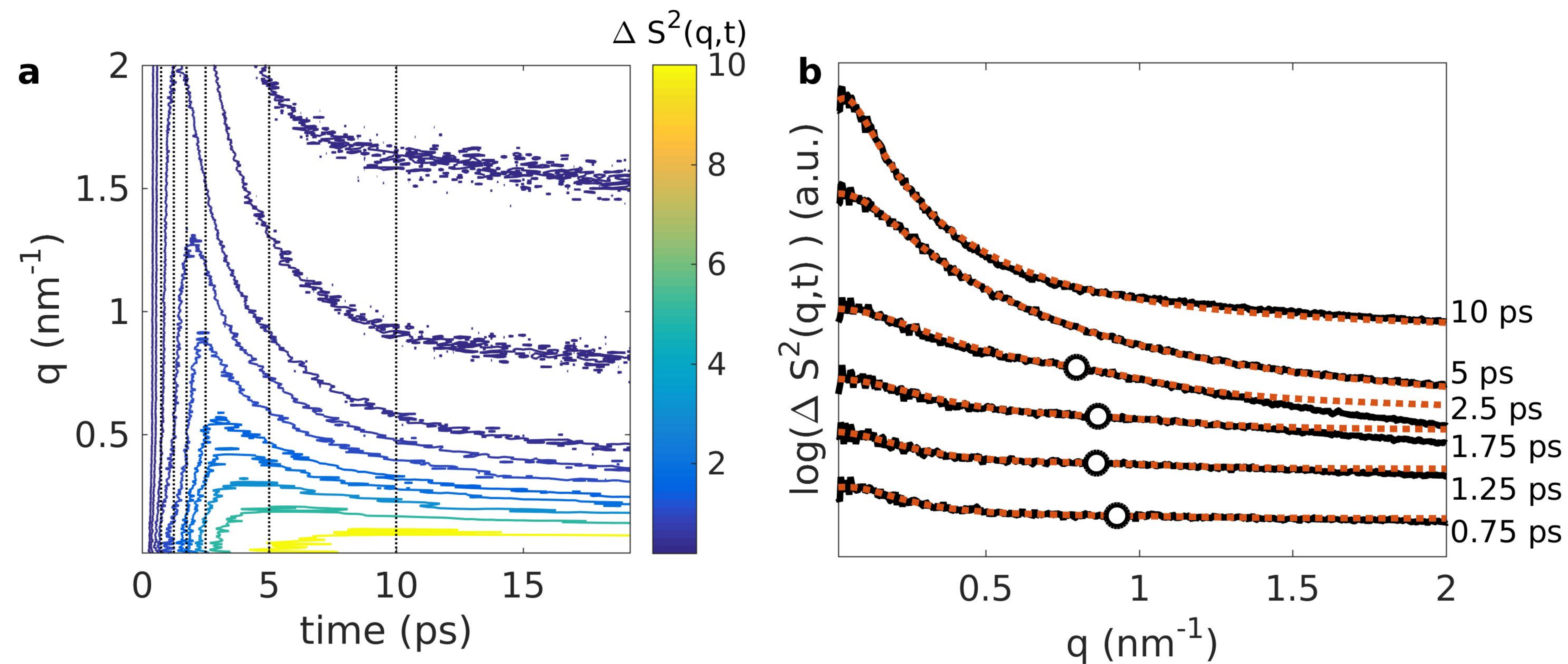




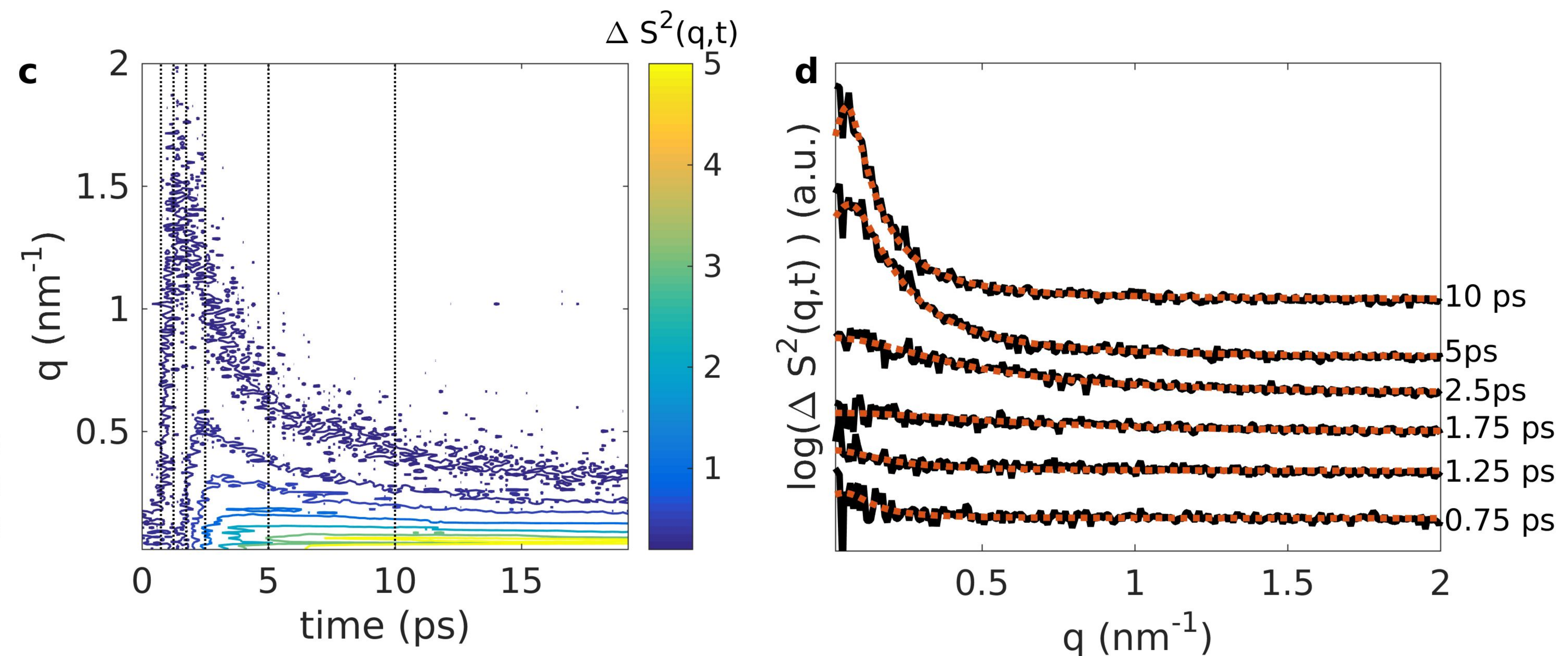
t

Atomistic

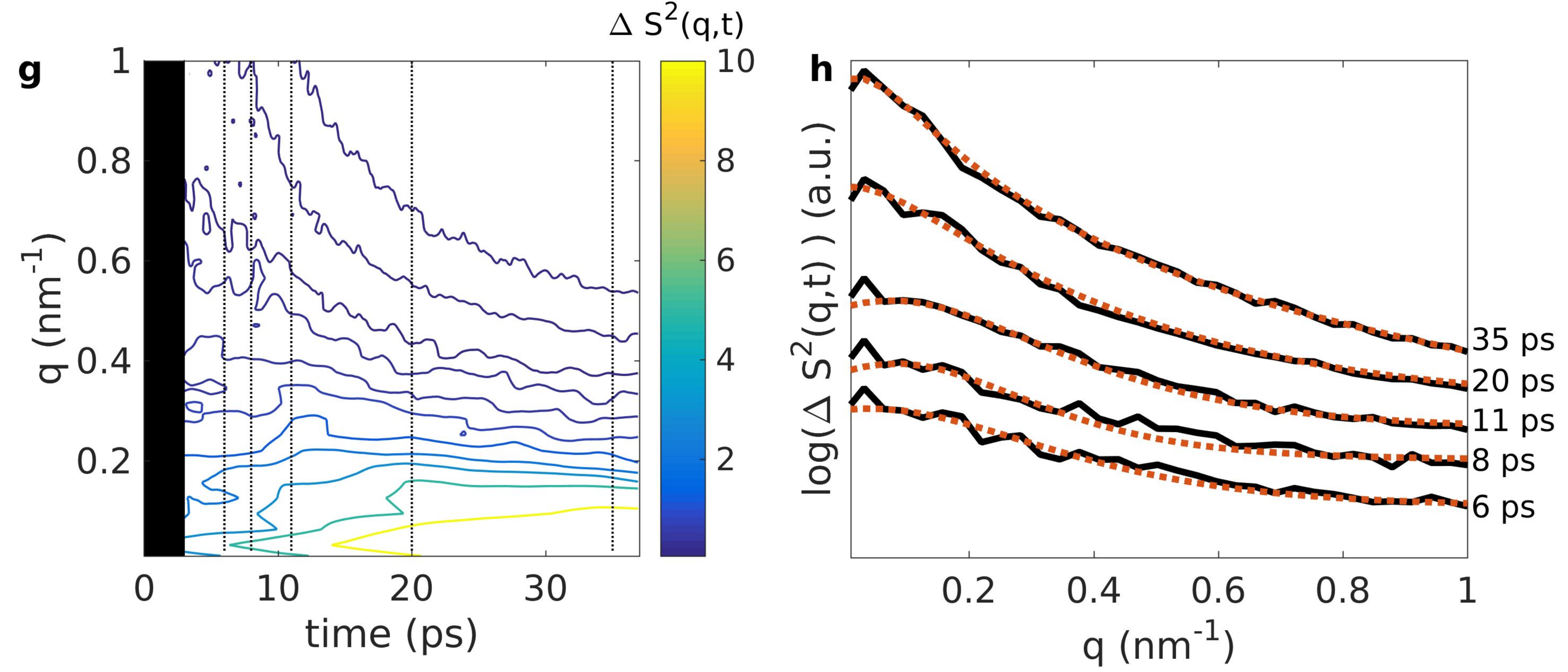
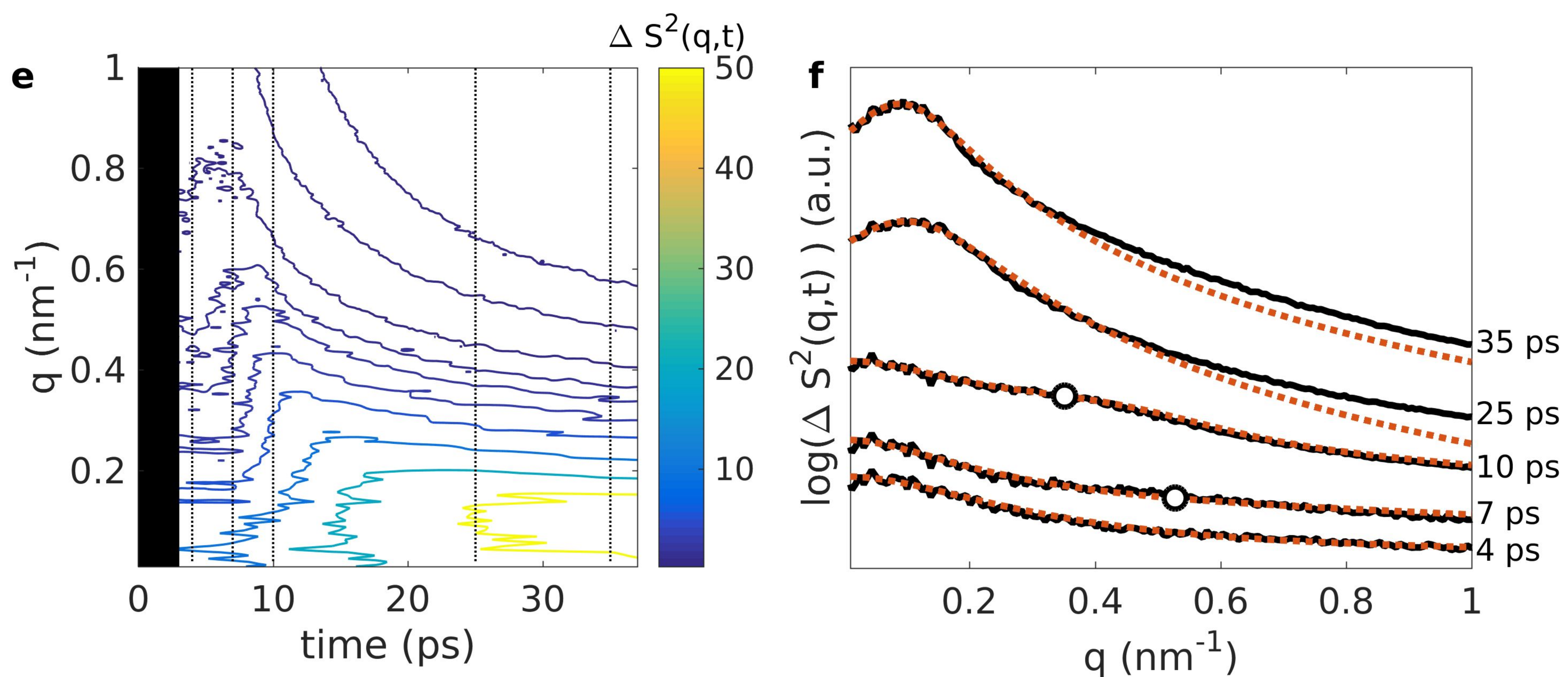
non-AOS

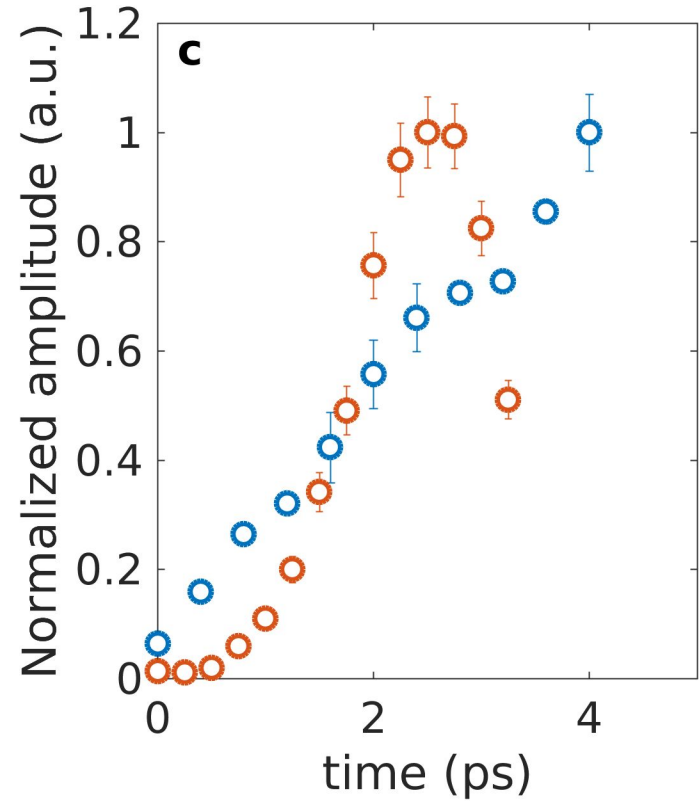
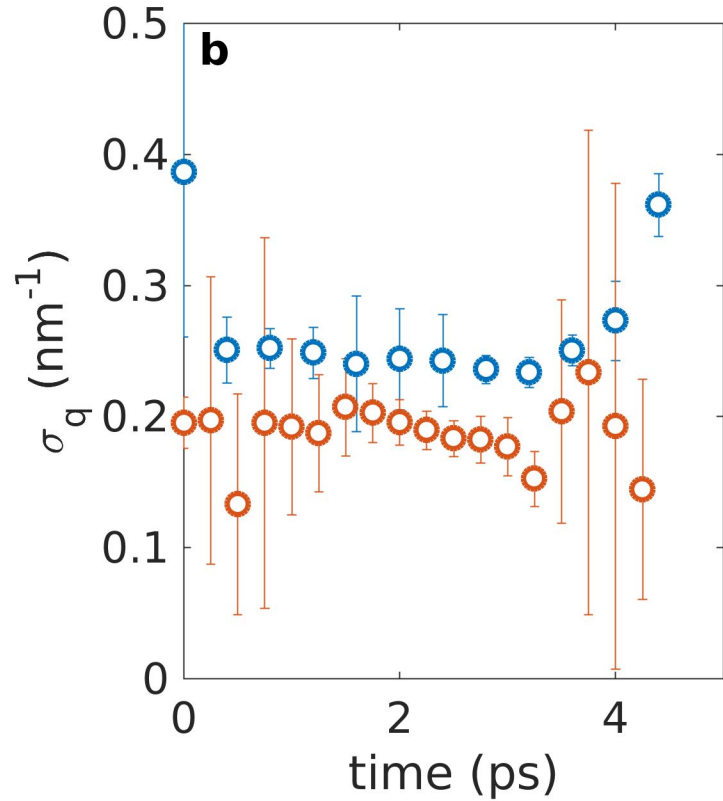
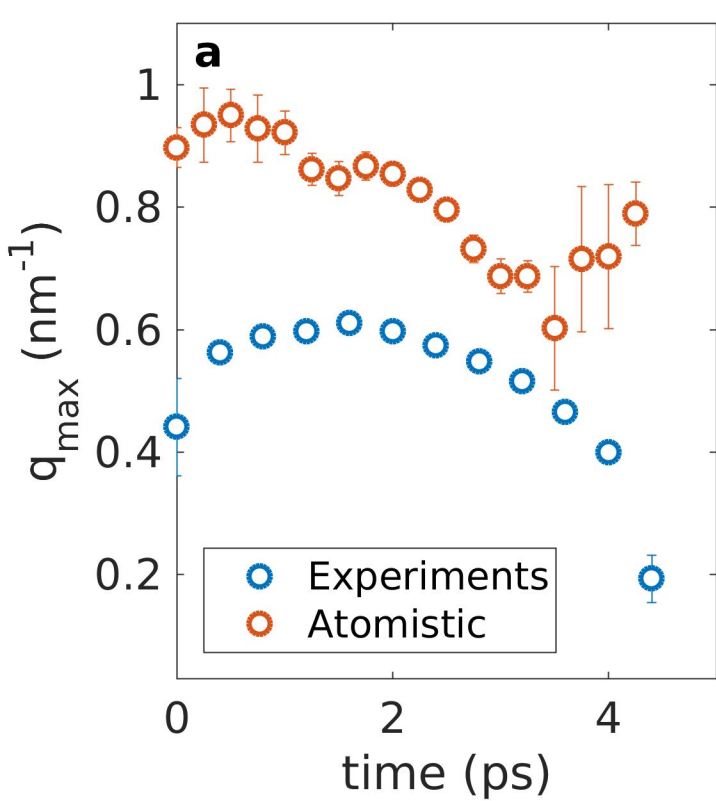


AOS



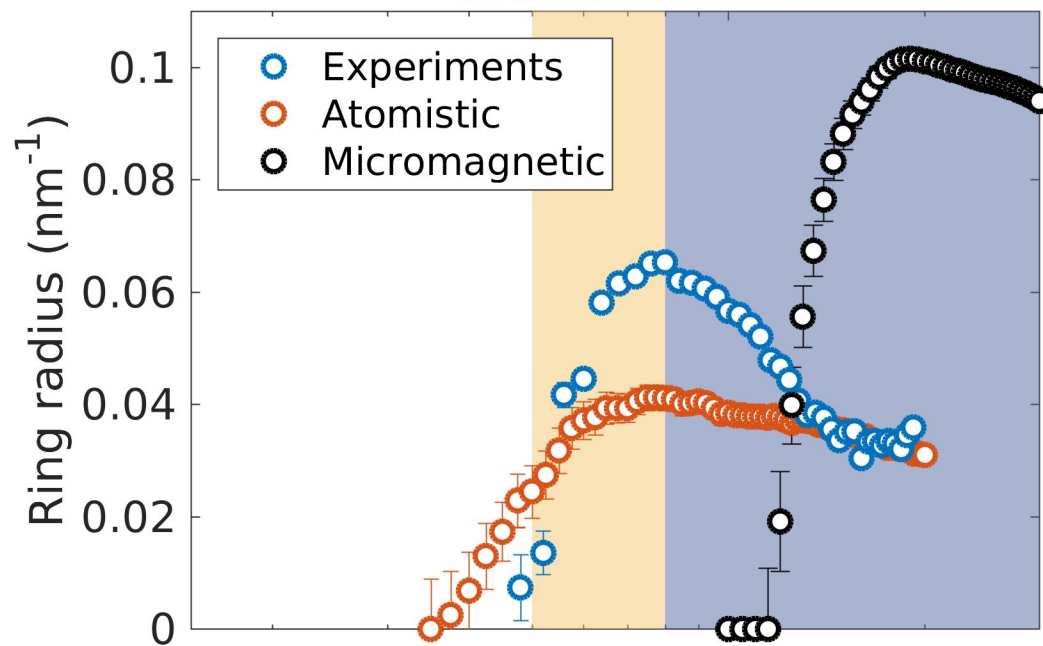
Micromagnetic





non-AOS

Localisation Coalescence

**AOS**

Localisation

